
8-2021

Investigation Of Trophon® 2 For High Level Disinfection Of Rigid Endorectal Mri Coils

Rebecca DiTusa

Follow this and additional works at: https://digitalcommons.library.tmc.edu/utgsbs_dissertations



Part of the [Medicine and Health Sciences Commons](#)

Recommended Citation

DiTusa, Rebecca, "Investigation Of Trophon® 2 For High Level Disinfection Of Rigid Endorectal Mri Coils" (2021). *Dissertations and Theses (Open Access)*. 1142.

https://digitalcommons.library.tmc.edu/utgsbs_dissertations/1142

This Thesis (MS) is brought to you for free and open access by the MD Anderson UTHealth Houston Graduate School at DigitalCommons@TMC. It has been accepted for inclusion in Dissertations and Theses (Open Access) by an authorized administrator of DigitalCommons@TMC. For more information, please contact digcommons@library.tmc.edu.

INVESTIGATION OF TROPHON® 2 FOR HIGH LEVEL DISINFECTION
OF RIGID ENDORECTAL MRI COILS

by

Rebecca Rose Feuer DiTusa, B.S.

APPROVED:

James Bankson, Ph.D.
Advisory Professor

Christopher Walker, Ph.D.

Jason Stafford, Ph.D.

Sanjay Shete, Ph.D.

Gregory Ravizzini, MD

APPROVED:

Dean, The University of Texas
MD Anderson Cancer Center UTHealth Graduate School of Biomedical Sciences

INVESTIGATION OF TROPHON® 2 FOR HIGH LEVEL DISINFECTION
OF RIGID ENDORECTAL MRI COILS

A

Thesis

Presented to the Faculty of

The University of Texas

MD Anderson Cancer Center UTHealth

Graduate School of Biomedical Sciences

in Partial Fulfillment

of the Requirements

for the Degree of

Master of Science

by

Rebecca Rose Feuer DiTusa, B.S.
Houston, Texas

August, 2021

Dedication

I dedicate this to my family. I know you will be there for me no matter what, and that's the best gift in life I could ever ask for.

"I'll love you forever
I'll like you for always
As long as I'm living
My baby you'll be."

- Robert Munsch

Acknowledgments

I first want to thank my advisor Dr. James Bankson. There is absolutely, no way that I could sufficiently express to you the impact you have had on my life. I want you to know that I recognize that you are insanely busy with your research and with your family, and somehow found the time to be my mentor. You have continuously made me feel respected not only as a student, but as a person. Thank you for empowering me by saying, “what do you think? This is your project.” Someone so intelligent wanting to know what I thought, was exactly what I needed. Thank you.

Thank you to Dr. Christopher Walker and Dr. Keith Michel for spending hours after the work day helping me acquire data. I could not have done it without you. Your suggestions, your guidance, and your kindness have not gone unnoticed. In addition, thank you to James Carl for helping me with my inoculation experiments—your insight and knowledge about the bacteria experimentation was very helpful.

I want to thank my committee members Dr. James Bankson, Dr. Christopher Walker, Dr. Jason Stafford, Dr. Sanjay Shete, and Dr. Gregory Ravizzini for helping me through this fast-paced process. Your questions and suggestions were immensely helpful—they helped guide me and allowed me to understand my shortcomings.

I want to thank Dr. Kristy Brock for reaching out to me when I needed it most and continuing to be there for me.

I want to thank my classmates—I am so sad our Bachelor-watching and first-year-office-talks were cut short due to a pandemic. A special thank you to Barbara for being there for me for anything at any hour. Thank you to Fre’Etta for always sending me video messages and checking on me and the pups.

And of course, I want to thank my family. Thank you, Mom and Dad, for always being there for me. Thank you for always thinking of me and having my best interest in mind. Thank you, Mom, for being a superhero and always driving me to gymnastics. Thank you, Dad, for pushing me to be my best. Thank you to my brother, Mark, for being the silliest person I know, but also always there to talk through anything. Thank you to my sister Chloe, for still looking up to me and believing in me, even though I will never perfect my job as a big sister. I cannot fathom a life without you guys. I love you.

INVESTIGATION OF TROPHON[®] 2 FOR HIGH LEVEL DISINFECTION OF RIGID ENDORECTAL MRI COILS

Rebecca Rose Feuer DiTusa, B.S.

Advisory Professor: James Bankson, Ph.D.

Clinical Magnetic Resonance Imaging is most widely known for anatomical images with good image resolution and superb soft-tissue contrast. However, changes tumor metabolism may precede changes in gross size of the tumor. Newer studies present the use of ¹³C in MR imaging to interrogate tumor metabolism. With this additional information, not only can the size and makeup of a tumor be obtained, but also information about its metabolic characteristics. An increase in glucose uptake and production of lactate in the presence of oxygen—*aerobic glycolysis*—identifies abnormal metabolism, and hence a potential increase in tumor aggressiveness.

Traditional ¹H MRI of the prostate is carried out using a disposable endorectal coil. Reusable intracavitary instruments, such as ¹H and ¹³C/¹H rigid endorectal coils, are classified as ‘semi-critical devices’ and must be processed by high-level disinfection (HLD) between uses. Current methods of HLD are based on chemical immersion. Consequently, the number of clinics implementing this HLD process is highly dependent on availability to significant investment of infrastructure and specifically trained staff. If clinics could feasibly perform and document HLD processing without such high demands, adopting the standards required by the JCAHO for reusable endorectal coils would become more attainable.

The trophon[®] 2 system is an FDA approved device for carrying out HLD on reusable ultrasound probes. This device is small enough to sit on a tabletop and can also easily

document HLD processing. Although trophon[®] 2 has been cleared for use with ultrasound probes, it has not been cleared for MRI coils.

The purpose of this work was to assess the viability of using trophon[®] 2 for HLD of a rigid endorectal coil. We hypothesize that high level disinfection of rigid endorectal coils, by means of trophon[®] 2, allows for complete disinfection of the biological safety level 1 organisms advised by United States Pharmacopeia and the National Formulary, and no degradation of the coil's signal to noise ratio performance.

Table of Contents

Approval Page.....	i
Title Page.....	ii
Dedication.....	iii
Acknowledgments.....	iv
Abstract.....	vi
Table of Contents.....	viii
List of Illustrations.....	x
List of Tables.....	xv
Chapter 1.....	1
1.1 Motivation.....	1
1.2 Background.....	3
1.2.1 MRI Basics.....	3
1.2.1.1 Basic Science.....	3
1.2.1.2 MRI Features.....	4
1.2.1.3 K-Space.....	7
1.2.1.4 Pulse Sequence.....	7
1.2.2 MR Image Properties.....	9
1.2.2.1 Signal to Noise Ratio.....	9
1.2.2.2 Center Frequency of the Receiver Coil.....	10
1.2.3 MRI Quality Control.....	10
1.2.4 Endorectal Coil.....	11
1.2.5 Carbon MRI.....	12
1.2.6 High Level Disinfection.....	13
1.2.6.1 Chemical Immersion.....	14
1.2.6.2 Trophon® 2.....	14
1.3 Hypothesis and Specific Aims.....	15

1.3.1 Hypothesis	15
1.3.2 Specific Aims.....	15
Chapter 2	16
2.1 Method and protocol for evaluating functionality of a rigid endorectal coil	16
2.1.1 Setup Reproducibility	16
2.1.2 Phantoms	18
2.1.3 Pulse Sequence	19
2.1.4 SNR Calculation	20
2.2 Method and protocol for evaluating complete disinfection of bacteria from a rigid endorectal coil	21
2.3 Method and protocol for assessing rigid endorectal coil properties with respect to trophon® 2 HLD.....	25
2.3.1 Coil Baseline Assessment	25
2.3.2 trophon® 2 Protocol	27
Chapter 3	29
3.1 Experimental results from HLD of an inoculated rigid endorectal coil	29
3.2 Experimental results from assessing rigid endorectal coil properties with respect to trophon® 2 HLD.....	35
Chapter 4	49
4.1 Impact of trophon® 2 HLD on a reusable endorectal MRI coil.....	49
4.2 Future Directions	51
Appendix A.....	54
Automatic Pre-Scan Values	54
Bibliography	58
Vitae.....	61

List of Illustrations

Figure 1 A) represents the variability of spin vectors when not in the presence of a strong magnetic field—there is no bulk magnetization produced. B) demonstrates the aligning behavior of a spin-system when introduced to a strong external magnetic field, B_0 . C) displays the effect of a spin system due to a transmission coil emitting RF pulses, tipping the spins into the xy -plane. D) shows the behavior of a system favoring the lowest energy state—once the transmit coil is turned off, the spins align back to the external B_0 -field, which is measured with a receiver coil..... 5

Figure 2: GE ^1H rigid endorectal coil.....11

Figure 3: 3D printed structure holding the phantom and rigid endorectal coil. A) Outlined in black represents the placement of the rigid endorectal coil, which is placed reproducibly with respect to the phantom (outlined in green). B) depicts the insertion of the 50 mL conical tube within the 3D print, as well as the fiducial mark for aligning the sample within the magnet’s bore, and C) illustrates the placement of the endorectal coil within the 3D printed structure.17

Figure 4: Acrylic stand positioned on the MRI table. Reproducible setup ensured with consistent stand placement; the stand interfaces where a head coil is placed for patient imaging and is secured closest to the coil’s base. The 3D printed structure is placed atop the stand, secured in place with a recess of acrylic.18

Figure 5: Depiction of the 9 axial image slices acquired, each division is 5 mm.....19

Figure 6: Row 1 depicts the signal image of slices 3, 4, 5, 6, and 7. Row 2 illustrates the 6 thresholds of intensity, with the dark blue representing the noise, and therefore not included in the signal measurements for SNR calculations. Row 3 demonstrates the noise image acquired with the 189x189 pixel noise ROI.....21

Figure 7: Trial 1 involved LLD of the coil prior to inoculation with the use of a Clorox disinfection wipe. Then the coil was inoculated with the four bacteria on the coil at location 1, location 2, location 3, and location 4. After inoculation, two tryptic soy agar plates made direct contact with the coil to ensure successful inoculation. Plate a contacted the superior location of the coil, testing for bacteria at Location 1 and 2, and plate b contacted the inferior section of the coil, testing for bacteria at Location 3 and 4. Following this step, the coil received HLD in the trophon[®] 2. After HLD, the coil was tested with two more plates to test for the presence of bacteria. This experiment was repeated three times to test reproducibility.23

Figure 8: Arrow indicating the line that ultrasound transducers are recommended not to pass for disinfection; however, the rigid endorectal coil is longer. Locations labelled 1, 2, 3, and 4 represent the area for which each inoculated sample was placed. Plate a represents bacteria in locations 1 and 2, while Plate b represent locations 3 and 4. A syringe was used to inoculate the coil, and an L-spreader was used to spread the bacteria on the coil.24

Figure 9: Image set-up for visual assessment of the coil. Red tape represents the field of view of each image; drawn on the paper are outlines of the coil to line up with. Tape colors green, purple, yellow, and orange specify the position of the coil's base depending on which angle of the coil is being imaged.26

Figure 10: A) represents the location of temperature measured before and after each HLD cycle B) Location of temperature measured before each HLD cycle.....27

Figure 11: Two options of rigid endorectal coil placement within the trophon[®] 2. Setup A requires the electronic casing to receive HLD—however, the electronic casing does not require HLD and may not be sealed as sufficiently as the coil and neck of the coil; setup B fails to provide HLD to the neck of the rigid endorectal coil. Because of this, this study uses setup A for HLD of the rigid endorectal coil28

Figure 12: Growth of *aspergillus brasiliensis*, *bacillus subtilis*, *candida albicans*, and *pseudomonas aeruginosa* for Trial 1 (row 1) and Trial 2 (row 2)—indicates the physical appearance of each organism as well as all organisms can grow in the experimental conditions defined29

Figure 13: For Trial 1.1, inoculation plate a showed successful inoculation of *aspergillus brasiliensis*, *candida albicans* and *bacillus subtilis*. Plate b presented growth from *bacillus subtilis* and *pseudomonas aeruginosa*. After HLD, there was no presence of any bacteria on the coil.....30

Figure 14: For Trial 1.2, inoculation plate a only showed successful inoculation of *pseudomonas aeruginosa*. Neither inoculation was successful for the inferior section of the coil, represented as plate b. After HLD, there was no presence of any bacteria on the coil. 31

Figure 15: For Trial 1.3, inoculation plate a there was a successful inoculation of *pseudomonas aeruginosa*. Neither inoculation was successful for plate b. After HLD, there was no presence of any bacteria on the coil.....32

Figure 16: For Trial 2.1, inoculation plate a presented successful inoculation of *aspergillus brasiliensis* and *bacillus subtilis*. *Pseudomonas aeruginosa* was successfully inoculated, presented on plate. After HLD, there was no presence of bacteria on plate a; however, plate b showed what appeared to be one CFU of *candida albicans*.33

Figure 17: For Trial 2.2, inoculation plate a showed successful inoculation of only *pseudomonas aeruginosa*. Plate b was showed that the *aspergillus brasiliensis* inoculation was successful. After HLD, there was no presence of bacteria on plate a; however, plate b showed what appeared to be five CFU of *candida albicans*.....33

Figure 18: For Trial 2.3, inoculation plate a, there was a successful inoculation of *pseudomonas aeruginosa* and *candida albicans*. Plate b showed no growth from any bacteria. After HLD, there was no presence of any bacteria on the coil.....34

Figure 19: Close-up of the bacterial growth of post HLD b-plates from Trial 2.1 and 2.2 as well as the candida albicans control plate for reference.....35

Figure 20: Signal images before and after 100 HLD cycles for Spin Echo (T_1 and T_2), GE-EPI (T_2^*), and GRE (T_2^*). No change in signal or artifacts is observed.36

Figure 21: Comparison of threshold as calculated by Otsu’s method for the water and the saline phantom.....36

Figure 22: Comparison of the water phantom’s baseline and post-100 HLD SNR_{mean} and SNR_{max} calculations.....37

Figure 23: Comparison of the saline phantom’s baseline and post-100 HLD SNR_{mean} and SNR_{max} data.37

Figure 24: Slice 5 of the water phantom, SNR_{mean} and SNR_{max} plots versus HLD cycle number. The slope each linear regressions is centered about zero at the 95% confidence level, with a p-value > 0.05.....40

Figure 25: Slice 5 of the saline phantom, SNR_{mean} and SNR_{max} plots versus HLD cycle number. The slope of each linear regression is centered about zero at the 95% confidence level, with a p-value > 0.05.....40

Figure 26: Coil images pre and post 100 trophon[®] 2 HLD cycles.....45

Figure 27: Images of the neck of the coil pre and post 100 trophon[®] 2 HLD cycles46

Figure 29: Chip on the base of the neck—present pre and post 100 HLD cycles.**Error!**

Bookmark not defined.

Figure 28: Small bubble formed on the tip of the rigid endorectal coil post 70 HLD cycles in the trophon[®] 246

Figure 30: Chip on the base of the neck of the coil, present before and after 100 HLD cycles47

Figure 31: Images of the electronics region of the coil pre and post 100 trophon[®] 2 HLD cycles.....47

Figure 32: A) Formation of bubbles from the paint on the casing of the electronics B) formation of bubbles on the paint of the casing of the electronics as well as under the caution sticker C) chips in paint on the electronic casing.....48

List of Tables

Table 1: Gyromagnetic Ratio of hydrogen-1 and carbon-13	4
Table 2: Prostate Phantom Samples	18
Table 3: Pulse sequence parameters for signal images used for QC baseline measurements. Group A was used for calculating SNR_{mean} and SNR_{max} ; both groups A and B were acquired for visualization of image properties. Note that for Group A, the k-space was zero-padded to obtain the 256x256 image size.	19
Table 4: Trial 1—placement of each bacteria on the endorectal coil for trophon® 2 HLD cycle	24
Table 5: Trial 2—placement of each bacteria on the endorectal coil for trophon® 2 HLD cycle	25
Table 6: One-sided paired t-test for each slice, comparing the 4 pre-HLD SNR data to the post-100 HLD data. The check represents the null hypothesis could not be rejected; the p-value is > 0.05 for each test.	39
Table 7: 95% confidence interval of slopes in Figure 24 and 25	41
Table 8: Estimated number of HLD cycles required to reduce the SNR by 10% of the original value—using the lowest value of slop in the 95% confidence level define in Table 7 with respect to the water phantom.	41
Table 9: Estimated number of HLD cycles required to reduce the SNR by 10% of the original value—using the lowest value of slop in the 95% confidence level define in Table 7 with respect to the saline phantom.	41
Table 10: Pre-HLD temperature of the electronic casing	42
Table 11: Pre-HLD temperature of the coil	43

Abbreviations

ATP – Adenine Triphosphate

CFU – Colony Forming Unit

DNP – Dynamic Nuclear Polarization

GE-EPI – Gradient Echo-Echo Planar Image

HLD – High Level Disinfection

HP – Hyperpolarization

JCAHO – Joint Commission on Accreditation of Healthcare Organizations

LLD – Low Level Disinfection

MRI – Magnetic Resonance Imaging

QC – Quality Control

RF – Radio frequency

ROI – Region of interest

SNR – Signal to Noise Ratio

TE – Time to Echo

TR – Repetition Time

USP-NF – United States Pharmacopeia and the National Formulary

WW – Watchful Waiting

Chapter 1

Introduction

1.1 Motivation

Within the last 40 years, the number of individuals in the United States diagnosed with prostate cancer per year has increased by greater than twenty percent, while the survival rate has increased by nearly thirty percent. These results correlate with the advancement in detection and therapy methods. However, the number of deaths from prostate are second only to lung cancer ('SEER*Explorer: An interactive website for SEER cancer statistics ').

Common forms of prostate cancer detection methods include digital rectal exams, testing prostate specific antigen levels, transrectal ultrasound imaging, positron emission tomography/computed tomography imaging studies, or magnetic resonance imaging (MRI) studies (Borley and Feneley 2009). Each of these techniques acquire information representative of a variety of the ways that cancer may present itself.

Prostate cancer treatment types vary by tumor type and include watchful waiting (WW), resection, radiation therapy, chemotherapy, hormone therapy, or a combination of these therapies (Denmeade and Isaacs 2002).

WW is an option for patients with either a short life-expectancy or small, non-aggressive forms of prostate cancer. This type of treatment involves periodically assessing the tumor growth using an invasive tumor-sampling diagnostic procedure; if disease progression is observed, other forms of therapy are prescribed. WW is a viable option for these patients due to the adverse effects caused by the other, more invasive forms of

therapy; because most prostate tumors progress very slowly, the patients' overall quality of life may be better if the tumor is left untreated (Bill-Axelsson et al. 2014).

Patients with large, aggressive tumors—or patients with non-aggressive tumors who opt out of WW—complete a full round of therapy before detection studies are acquired to determine treatment efficacy. Therefore, patients may undergo treatment for months without knowledge of changes due to progression or therapeutic response.

Magnetic resonance imaging (MRI) is a technique regularly employed for prostate tumor imaging. Differentiation between the signal and tumor is required for precise and accurate diagnosis. For the purpose of MR imaging of prostate tumors, an endorectal coil is used to increase the signal to noise ratio (SNR) and the contrast-to-noise ratio (CNR) between tumor and normal tissue. Current clinical endorectal coils are designed for hydrogen-based MR imaging and inflate once positioned near the prostate; inflation of the coil aids in reducing organ motion during image acquisition as well as an increased signal due to its close proximity to the prostate. Existing hygienic methods to prevent the spread of infection involve disposing of the endorectal coil after each use. This precaution is taken to ensure bacteria is not spread from one patient to another. Alternatively, rigid endorectal coils, currently for research purposes only, allow for an increase in SNR and less image distortion (Noworolski et al. 2008). However, disposal of this coil after each patient is not clinically or economically practical.

Recent advances in MRI involve the use of carbon-labelling to observe metabolic properties of tumors—based off the Warburg effect (Lunt and Vander Heiden 2011). Knowledge about metabolic properties of tissues aid in understanding disease status and progression (Kurhanewicz et al. 2019).

Current coils used in clinical MR imaging are tuned to the resonant frequency for hydrogen. To employ carbon-based MRI, a dual tuned coil is ideal; tuned for both hydrogen

and carbon. Dual tuned coils—like rigid, hydrogen tuned coils—are more complex and expensive to produce. Consequently one-time-use of these coils are not clinically practical.

The proposed method for disinfecting rigid endorectal coils is a lengthy process that requires specifically trained staff as well as a room dedication for the procedure. For clinical adoption of the rigid endorectal coils, an effective, efficient, and reproducible method for disinfection that does not compromise coil performance is required.

1.2 Background

1.2.1 MRI Basics

MRI is a commonly used method for anatomical imaging because it is a noninvasive procedure and offers excellent image resolution of soft tissues without the use of radiation.

1.2.1.1 Basic Science

Nuclei for ^1H and ^{13}C have an angular momentum quantum number, or spin, $s = \frac{1}{2}$. In the presence of a magnetic field oriented along the z-axis, the z-component of the nuclear spin angular momentum either align parallel ($m_s = +\frac{1}{2}$) or anti parallel ($m_s = -\frac{1}{2}$) to the external magnetic field, and the Zeeman energy difference between these states causes a shift in the distribution of spins and leads to bulk magnetization. The strength of this magnetization is proportional to the strength of the external magnetic field and inversely proportional to the temperature—which can be represented by the Boltzmann equation:

$$\frac{N_-}{N_+} = e^{-\frac{E}{kT}} \quad (\text{Eq. 1})$$

Where $\frac{N_-}{N_+}$ represents the number up spin-up over the number of spin-down particles, E represents the Zeeman energy difference, T is the temperature in kelvin, and k is the Boltzmann factor.

Not only do the spins align with or against the external magnetic field lines, they also precess around the field lines at the Larmor frequency (ω_0),

$$\omega_0 = \gamma * B. \tag{Eq. 2}$$

The Larmor frequency is proportional to the magnetic field strength (B) as well as the gyromagnetic ratio (γ) (Constantinides 2016). The gyromagnetic ratio values for ^{13}C and ^1H (Chen 2020) are listed in Table 1.

$\gamma_{(^1\text{H})}$	$42.58 \frac{\text{MHz}}{\text{T}}$
$\gamma_{(^{13}\text{C})}$	$10.71 \frac{\text{MHz}}{\text{T}}$

Table 1: Gyromagnetic Ratio of hydrogen-1 and carbon-13

1.2.1.2 MRI Features

The four main features in an MRI are the main magnet, body transmit coil, receiver coil, and gradient coils.

Before a patient is placed within the MRI for imaging, their nuclear spins are oriented randomly, forming no net magnetization (Figure 1A). When a patient is within the bore of the MRI, a large, external, static magnetic field, $B_0 \hat{z}$ causes the nuclear spins' distribution to shift, producing a net magnetization along the z-axis, M_z (Figure 1B).

The transmit body coil is within the bore of the magnet, surrounding the patient. The transmit coil produces a magnetic field (B_1) by emitting radio frequency (RF) pulses at ω_L . This excites the spin system, which tips magnetization away from the z-axis, to the transverse (xy) plane. For example, a 90° flip angle converts the magnetization from M_z to M_{xy} —magnetization only in the xy -plane (Figure 1C).

After the body transmit coil excites by means of RF pulses, the system relaxes back to the lowest energy state—back along the z-axis, M_z (Figure 1D). A receive coil detects the

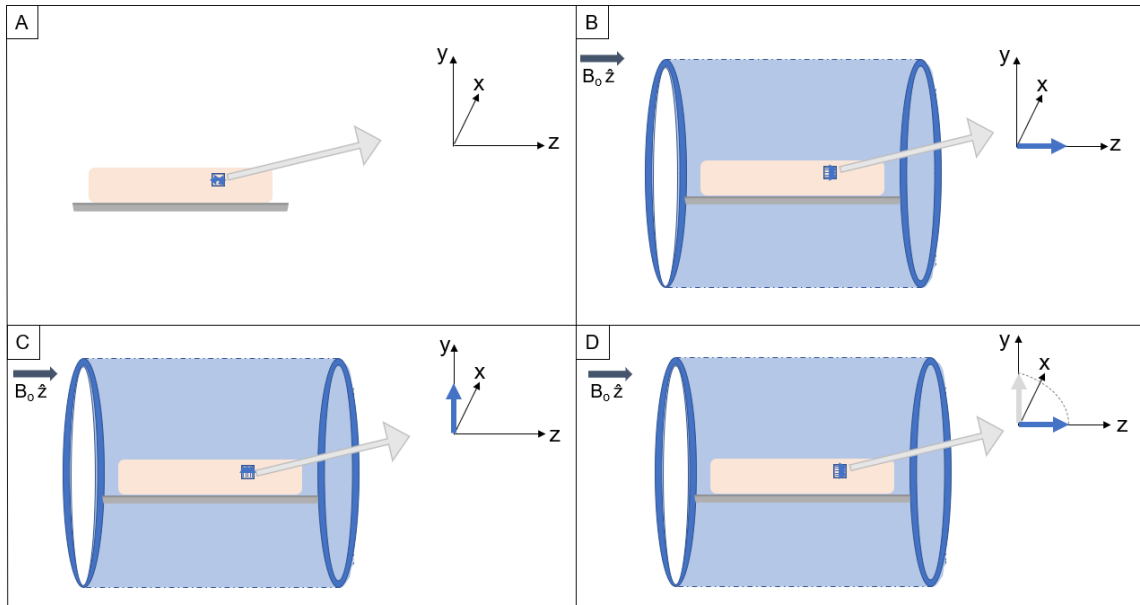


Figure 1 A) represents the variability of spin vectors when not in the presence of a strong magnetic field—there is no bulk magnetization produced. B) demonstrates the aligning behavior of a spin-system when introduced to a strong external magnetic field, B_0 . C) displays the effect of a spin system due to a transmission coil emitting RF pulses, tipping the spins into the xy -plane. D) shows the behavior of a system favoring the lowest energy state—once the transmit coil is turned off, the spins align back to the external B_0 -field, which is measured with a receiver coil.

precession of spins as they relax. Two time-constants (T_1 and T_2) are used to characterize the relaxation of the spin system. T_1 , the spin-lattice relaxation time constant, is the time required for 63 percent of the initial magnetization (M_0) to recover to the z -axis,

$$M_z = M_0 * (1 - e^{-\frac{t}{T_1}}); \quad (\text{Eq. 3})$$

T_2 , the spin-spin relaxation time constant, is the time for 63 percent of M_0 in the xy -planes to decay due to dephasing of spins,

$$M_{xy} = M_o * e^{-\frac{t}{T_2}}. \quad (\text{Eq. 4})$$

The signal measured directly relates to the precession of spins, which causes a time-varying magnetic field that cuts through the receiver coil employed during MRI data acquisition. Although a receiver coil exists within the bore of the magnet, image quality may be improved with the use of a surface coil. A surface coil is a small receiving coil that is placed within the bore of the magnet, near the organ of interest. This decreased distance of the coil increases the relative signal obtained from the organ of interest, to signal and noise received from the entire body.

Additionally, there are three gradient coils that vary the magnetic field strength along the x, y, and z direction—allowing for slice selection, phase encoding, and frequency encoding. The gradient coils produce a magnetic field that is linear in a given direction and adds to the external magnetic field, B_o . For example, if axial images are acquired, a slice select gradient adds spatial dependence to Equation 2, which is done with a linearly dependent magnetic field gradient along the z-direction, G_z . This affects the frequency at which the spin system precesses with varying location along the z-axis. The location of the excited volume can be specified by the center frequency of the excitation pulse—as only excitation occurs of spins precessing at the same frequency as the RF pulse. In addition, the size of the slice depends on the bandwidth of frequencies used to excite the sample. The relationship between position and frequency can be described by Equation 5:

$$\omega_z = \gamma(B_o + z * G_z(t)), \quad (\text{Eq. 5})$$

For a thicker slice, a larger bandwidth of RF pulses is emitted, which is related to the strength of the slice selecting gradient and the slice location. In addition, within that one slice, the phase-encoding and frequency-encoding gradients are applied orthogonal to the

slice selection direction to differentiate where, within the volume defined by the slice, magnetization is precessing (Constantinides 2016).

1.2.1.3 K-Space

RF pulses are used to manipulate bulk magnetization, and the signal that is subsequently measured is encoded by frequency and phase—rather than directly measuring the spatial location, like many other imaging modalities. Frequency encoding is achieved with the use of a gradient, for example linearly increasing along the x-direction, G_x . Along this x-axis, the precession of spins is dependent on the strength of the applied gradient. Then for phase-encoding, a gradient orthogonal to the frequency encoding gradient, therefore in this example, along the y-axis, is employed to alter the spatial phase distribution in that direction by the strength and duration of the gradient, represented by the following equation:

$$k_y = \gamma \int_0^t G_y dt. \quad (\text{Eq. 6})$$

Where k_y is the spatial frequency, γ is the gyromagnetic ratio, G_y is the gradient strength, and t is the amount of time the gradient is applied. To spatially encode received signal, the phase encoding pulses occur between excitation and signal readout, and frequency encoding gradients are applied during signal readout.

The Fourier Transform (FT) of k-space is taken to transform the data from the spatial frequency domain into image space (Brown et al. 2014). To prevent aliasing artifacts from occurring in the final image, a variety of phase encoding gradients are utilized to sufficiently sample all of k-space (Constantinides 2016).

1.2.1.4 Pulse Sequence

A pulse sequence is a user-defined set of instructions, identifying the timing and strength of gradient and RF pulses applied, for MRI data acquisition. Basic features of a pulse sequence include one or more RF pulses, slice selection gradients, phase encoding gradients, and frequency encoding gradients. Depending on the order and timing of the RF transmissions, gradients, and signal readout, T_1 or T_2 contrast between tissues can be manipulated by the pulse sequence. Therefore, contrast between anatomical structures may be modified depending on the pulse sequence parameters employed to achieve, for example, T_1 -weighted or T_2 -weighted contrast.

After initial RF pulses and gradients are applied to excite and spatially encode the spin system, signal is measured at a point of maximum phase coherence—known as an echo. Spins precess at different frequencies based on their Larmor frequency and local inhomogeneities within the system; measurable signal, an echo, occurs when spins coherently add. The time between the initial RF pulse and the formation of the echo is known as the time to echo (TE). MRI pulse sequences are typically repeated multiple times with varying gradients to fill k-space. The time between the first RF pulse and the RF pulse following the measured echo, is known as the repetition time (TR). TE and TR are parameters that can be defined by the user, directly related to image-weighting properties. For example, imaging with a short TE and TR would produce a T_1 weighted image, whereas a long TR and TE would be utilized for a T_2 weighted image (Constantinides 2016).

Signal formation can be accomplished in multiple ways. For example, after the initial RF pulse, spin echo (SE) pulse sequences use a second RF pulse to refocus signal, whereas gradient echo (GRE) pulse sequences use a gradient. Of note, transverse signal relaxation in GRE sequences reflect inhomogeneity effects of the magnetic field (T_2^*) as well as the spin-spin dephasing interactions (T_2).

If fast image acquisition is required, gradient echo-echo planar imaging (GE-EPI) may be utilized; GE-EPI uses a single excitation, along with many small phase encoding gradients—blips—and rapidly oscillating readout gradients to fill k-space (Constantinides 2016).

1.2.2 MR Image Properties

MR image quality is related to many factors; the main properties that effect the image quality related to this work are signal to noise ratio (SNR) and center frequency of the receiver coil.

1.2.2.1 Signal to Noise Ratio

SNR compares the amount of signal measured in a region of interest, to the background noise,

$$SNR_{Gaussian} = \frac{S}{\sigma}. \quad (Eq. 7)$$

Where S is signal in the region of interest (ROI) and σ is the standard deviation of the noise. The dominant source of noise produced in MR images is thermal noise, which may arise from the coil, electronics, or tissue. Thermal noise in raw data and spectral or spatial transform domains have a Gaussian distribution. However, when evaluating the magnitude of the noise data in regions of low signal, the distribution is no longer Gaussian, but instead Rician. To correct for Rician noise (Gudbjartsson and Patz 1995),

$$SNR_{Rician} = \frac{S}{\sigma} * 0.655 = SNR_{Gaussian} * 0.655. \quad (Eq. 8)$$

Because of the increased ratio between signal and the standard deviation of noise with increasing SNR , the sensitivity and specificity of image analysis also increases, as does the contrast-to-noise ratio between tissues. Other factors that may affect the SNR include the

strength of B_0 , the coil sensitivity pattern, and pulse sequence parameters (Bushberg and Boone 2011).

According to Price et al. (2015), surface coils present a non-uniform sensitivity, and slight changes in experimental set-up may affect SNR measurements. Therefore, both SNR_{mean} and SNR_{max} of a surface coil are beneficial parameters to calculate for quality control testing—where S in Equation 7 represents the *mean* and *max* signal in the ROI, respectively.

1.2.2.2 Center Frequency of the Receiver Coil

The frequency at which the spin system precesses in the presence of a magnetic field—dependent on the Larmor frequency (Table 1)—is the center frequency for which the receiving coil is tuned to. If the receiving coil is tuned correctly, the largest signal, and therefore largest SNR, will be measured. If the center frequency is mis-tuned, a decrease in signal and SNR will be measured (Gruber et al. 2018). For example, if the receive coil is tuned for detecting signal from ^1H , then no ^{13}C signal can be measured; similarly, if tuned for ^{13}C , no signal is detected from ^1H nuclei.

1.2.3 MRI Quality Control

For optimal diagnostic ability of an MRI, all equipment must be functioning properly. For this reason, quality control (QC) tests are frequently completed; these are procedural tests to ensure equipment is performing within a specified performance level. To determine whether a piece of equipment is functioning properly, a measurement protocol is established, and periodic measurements are compared to the baseline measurements. A reproducible setup is important to limit confounding factors that may affect measurements of the device under test.

Table position, artifact evaluation, and transmitter gain are a few examples of equipment that require weekly QC testing by radiological technologist. With regular QC, slight changes in performance can be addressed before image quality, or worse, clinical evaluation of patient scans are affected (Price et al. 2015). If any of these parameters being testing for QC are found to function outside of an expected performance range, the medical equipment may need to be removed for service prior to further use.

1.2.4 Endorectal Coil

For MRI prostate imaging, an endorectal coil—a type of surface coil—is placed within the rectum of the patient, where the coil is located posterior to the prostate. The current endorectal coil used for clinical MR prostate exams are expandable endorectal coils. These are one-use coils that are inflated once placed into the rectum.

Alternatively, rigid endorectal coils (*Figure 2*), currently only for research studies, do not inflate and are not disposable.



Figure 2: GE ¹H rigid endorectal coil

A study by Powell et al. (2014) tested the differences between a rigid and an inflatable endorectal coil, including image quality and patient comfort. This study reported that there was less discomfort, better structure identification, and less prostate distortion when using a rigid endorectal coil.

1.2.5 Carbon MRI

Although only hydrogen-based MR images are used in a clinical setting, the addition of carbon-based imaging may further advance the understanding of disease staging or provide earlier indications of response to therapy.

The production of energy in the human body commonly begins with the conversion of glucose ($C_6H_{12}O_6$) to pyruvate ($C_3H_4O_3$)—a process known as glycolysis. If oxygen is present, pyruvate will be broken down by means of aerobic respiration; if oxygen is not present, pyruvate will be broken down by anaerobic respiration.

Aerobic respiration results in the production of carbon dioxide, water, and 36 molecules of adenine triphosphate (ATP); this process takes hours to occur. Anaerobic respiration results in the production of lactate ($C_3H_6O_3$) and two molecules of ATP; although this process produces less energy, each cycle is completed in less than a minute—making the process at least 60 times faster (Marieb and Hoehn 2007).

However, cancerous cells tend to undergo aerobic glycolysis, also known as Warburg effect. Because tumor cells proliferate quickly, they adapt and obtain the ability to undergo aerobic glycolysis—anaerobic respiration, even in the presence of oxygen. Using carbon-based MRI, the production of lactate from pyruvate can be observed, and the Warburg effect can be quantified—furthering the understanding of disease progression (Kurhanewicz et al. 2019).

Carbon based imaging is not currently performed in the clinic due to two main reasons: the net magnetization of carbon is weak at room temperature and a carbon-tuned receiver coil is required.

Using hyperpolarization (HP), the signal from ^{13}C can be briefly increased—allowing for MR imaging. For example, dynamic nuclear polarization (DNP) is a process that

increases the signal from ^{13}C by more than 10,000-fold. Increased signal is produced by cooling the sample in the presence of a polarizing radical, microwaves and a strong magnetic field (Jones et al. 2018). This method can be used to produce ^{13}C labeled pyruvate that can be injected into the patient creating a measurable ^{13}C net magnetization (Kurhanewicz et al. 2019). The ^{13}C HP signal decays within minutes, and dynamic HP MRI data is generally acquired using a GE-EPI sequence (Gordon et al. 2018).

To image anatomical structures as well as metabolic rate of tissue, a coil tuned for both ^1H and ^{13}C , known as a dual tuned coil, is required. A rigid, dual tuned coil has been produced for research purposes but has not yet been cleared for use in the clinic. In addition, the large cost to construct rigid dual tuned coils, has, thus far, made it impractical to clinically implement these as a one-use device (Haider et al. 2014).

1.2.6 High Level Disinfection

There are different levels of disinfection required by the Joint Commission on Accreditation of Healthcare Organizations (JCAHO). For endorectal coils and other semi-critical devices, high level disinfection (HLD) is required due to contact with mucous membranes or non-intact skin. According to United States Pharmacopeia and the National Formulary (USP-NF), microorganisms commonly required for sterility testing include staphylococcus aureus, bacillus subtilis, pseudomonas aeruginosa, clostridium sporogenes, candida albicans, and aspergillus brasiliensis (The United States Pharmacopeia 1979). Clostridium sporogenes is an obligate anaerobe and therefore cannot live in the presence of oxygen (Vennesland and Hanke 1940); because of this, clostridium sporogenes was not included in this study. In addition, staphylococcus aureus ('Basics of Biosafety Level 2'), a high-risk organism, was omitted from this study as well for precautionary purposes.

1.2.6.1 Chemical Immersion

The current proposed method for HLD of a rigid endorectal coil is chemical immersion. Chemical immersion is a long and tedious process which requires specialized trained staff as well as significant infrastructure in the form of a room dedicated to this HLD process (Pyrek). This greatly limits the number of clinics willing to implement HLD necessary for the repeated use of a rigid endorectal coil.

1.2.6.2 Trophon® 2

An endorectal transducer is a medical device used for ultrasound imaging of the prostate. Because this probe is placed within the body to image, HLD must be carried out in between patients. However, instead of chemical immersion, HLD of these probes are clinically implemented with the use of trophon® 2. trophon® 2 is small enough to sit on a table, disinfects using heat (60°C) and hydrogen peroxide, has a disinfection cycle lasting only seven minutes, and is effective against a wide range of pathogens. In addition, ultrasonic vibrations of the hydrogen peroxide within the chamber of the trophon® 2 produce small, free-radicals that are able to disinfect all small spaces that may contain bacteria ('Trophon Traceability and Storage Solution').

According to the manufacturer of trophon® 2, Nanosonics Ltd, about 3,000 facilities in the United States have adopted the use of trophon® 2 for ultrasound transducer HLD due to its ease of use; this suggests that endorectal coil HLD via trophon® 2 also has the potential for wide clinical adoption. However, MRI endorectal coils have not been tested for compatibility with trophon® 2.

1.3 Hypothesis and Specific Aims

1.3.1 Hypothesis

We hypothesize that HLD of rigid endorectal coils, by means of trophon[®] 2, allows for complete disinfection of the biosafety level 1 organisms advised by the USP-NF, with no degradation of the coil SNR or imaging capabilities.

1.3.2 Specific Aims

SPECIFIC AIM 1:

Design QC methods to assess functionality of a rigid endorectal coil.

SPECIFIC AIM 2:

Determine if trophon[®] 2 can reliably disinfect a variety of bacteria from the rigid 1H endorectal coil.

SPECIFIC AIM 3:

Assess whether trophon[®] 2 can be used for HLD of reusable MRI endorectal coils, without compromising SNR.

Chapter 2

Materials and Methods

To evaluate the ability of trophon® 2 to achieve HLD of a rigid endorectal coil without degrading the coil's SNR capabilities, three objectives were set. First, a procedure was developed to evaluate the SNR performance of the rigid endorectal coil; followed by experimentation of complete disinfection of the coil; and finally, assessing the coil's performance and physical properties after ten sets of ten consecutive HLD cycles.

2.1 Method and protocol for evaluating functionality of a rigid endorectal coil

QC tests are highly controlled, reproducible tests to evaluate equipment performance. Any variability in setup may alter resulting measurements, highlighting the importance of established and well controlled routine testing. In addition, acceptable variability of each QC test is essential for assessing test outcomes.

In this section, QC methods to assess the functionality of the rigid endorectal coil are broken down into four categories: setup reproducibility, phantoms, pulse sequences, and SNR calculation methods.

2.1.1 Setup Reproducibility

Surface coil sensitivity decreases with radial distance from the coil—meaning, for reproducible testing, the placement of a prostate phantom with respect to the coil should be constant. To achieve constant placement, consistent with the spatial relationship of a

prostate imaged by a rigid endorectal coil, a 3D printed design was created to hold a 50 mL conical tube in a fixed position, directly above the coil (Figure 3).

The position of the sample within the bore of the MRI magnet

was also taken into consideration. Ideally, within the bore, there is homogeneous magnetic field; however, in practice, it is unrealistic to assume perfect external B-field homogeneity.

Because of this, the position of the sample and coil within the bore of the MRI was controlled by constructing an MRI-compatible stand. The stand interfaces directly to the MRI table at a specific position and holds the 3D printed coil/phantom structure at the center of the bore.

Using the rigid endorectal coil base, the coil was held at the correct height,

positioned within the 3D printed structure, directly below the phantom (Figure 4). To

guarantee a reproducible setup, a fiducial reference point for landmark was made at the top of the 3D printed structure, shown in Figure 3B.

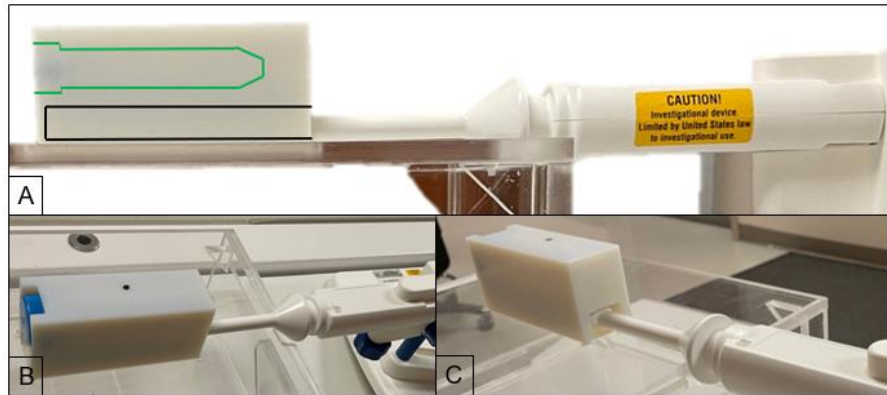


Figure 3: 3D printed structure holding the phantom and rigid endorectal coil. A) Outlined in black represents the placement of the rigid endorectal coil, which is placed reproducibly with respect to the phantom (outlined in green). B) depicts the insertion of the 50 mL conical tube within the 3D print, as well as the fiducial mark for aligning the sample within the magnet's bore, and C) illustrates the placement of the endorectal coil within the 3D printed structure.

2.1.2 Phantoms

Two prostate phantoms were utilized to test the baseline performance of the coil: Milli-Q water and a saline solution sample. The saline sample is a mix of 50% of Milli-Q water and 50% saline solution (Table 2). 50 mL of each sample was contained in a 50 mL conical tube—to fit within the set-up described in the previous section.



Figure 4: Acrylic stand positioned on the MRI table. Reproducible setup ensured with consistent stand placement; the stand interfaces where a head coil is placed for patient imaging and is secured closest to the coil's base. The 3D printed structure is placed atop the stand, secured in place with a recess of acrylic.

The signal intensity measured by the receiving coil is expected to be dependent on the chemical makeup of the sample of interest. Here, the water sample has a lower ion density than the saline solution, and therefore has a lower conductivity. The increased conductivity in the saline solution increases sample losses. Thus, the saline sample more closely approximates observations in a patient, where noise is induced both by coil and sample losses (Xu et al. 2006). Hence, a decreased signal intensity due to coil failure may be more significant and noticeable in the a the low-conductivity water sample, before being apparent in the saline sample.

Prostate Phantoms	
Water Sample	50 mL H ₂ O
Saline Sample	50 mL H ₂ O 225 mg NaCl

Table 2: Prostate Phantom Samples

2.1.3 Pulse Sequence

A wide variety of pulse sequences are used for MR imaging. In this study, SE and GRE pulse sequences were employed, as these two are the basis for the most advanced sequences. Because GE-EPI is often used for ^{13}C imaging, GE-EPI images were acquired as well. Axial images of each phantom were acquired with the minimum slice thickness of 5 mm and a 5 mm skip was added to prevent cross-slice excitation. As presented in Figure 5, in total there were nine slices encompassing the length of the sample, with 1 cm between each slice center. Image acquisition parameters are noted below in Table 3.



Figure 5: Depiction of the 9 axial image slices acquired, each division is 5 mm.

Group	Pulse Sequence		Slice Thickness	TR	TE	Phase/ Frequency	Bandwidth	Image Size	Flip Angle
A	SE	T1	5.0	300	20	128	15.63	256x256	--
		T2	5.0	3000	100	128	15.63	256x256	$\theta_{refocus} = 125^\circ$
	GRE	T2*	5.0	120	Min Full	128	31.25	256x256	$\theta_{excite} = 90^\circ$
B	GE-EPI		5.0	500	Min Full	64	100	64x64	--

Table 3: Pulse sequence parameters for signal images used for QC baseline measurements. Group A was used for calculating SNR_{mean} and SNR_{max} ; both groups A and B were acquired for visualization of image properties. Note that for Group A, the k-space was zero-padded to obtain the 256x256 image size.

From the images acquired, both Group A and B from Table 3, a visual assessment was completed; this is important for evaluating any changes in artifacts or signal intensity of future images.

2.1.4 SNR Calculation

To quantify the signal measured by the receiving endorectal coil, the mean signal-to-noise ratio, SNR_{mean} , and the maximum signal-to-noise ratio, SNR_{max} , were calculated. For both the water and saline phantom, only slices three through seven—the middle five slices—of each SE and GRE image were processed due to the limited extent of uniform coil sensitivity and potential susceptibility artifacts on the edge slices. Both SNR_{mean} and SNR_{max} were calculated because, as mentioned previously, surface coils present a non-uniform sensitivity, and slight changes in experimental set-up may affect SNR measurements.

Because these images are to be used for SNR calculations, each signal image acquisition was preceded by an automatic pre-scan where the center frequency, receive gain, and transmit calibration values were noted, to ensure consistency. These values are recorded in Appendix A.

Following the collection of each signal image, a noise image was acquired. The center frequency and receive gain were held constant, while the RF pulse amplitudes were set to zero, creating a condition where there was no excitation of the sample and ensuring a pure observation of image noise.

Because the signal strength is location dependent in the signal images (Figure 6, row 1), the signal ROI must be consistently defined. For this reason, Otsu's threshold algorithm was used to differentiate the signal from the noise; to achieve different levels of thresholds, iterations are made until the standard deviation of each group is at a minimum (Bangare et al. 2015). Five signal threshold levels and one noise threshold were defined for each slice

(Figure 6, row 2), where all signal voxels represent the signal ROI for SNR calculations. Five threshold levels were defined because this best defined the phantom versus noise. In addition, viewing the different thresholds within the phantom could be informative based on how the coil is functioning. For each noise image collected, a 189x189 voxel ROI drawn in the center of each noise image (Figure 6, row 3), which was used to calculate the standard deviation of the Rician noise. Of note, for Group A, there were 128 phase and frequency encoding gradients, but k-space was zero-padded in order to obtain a final image size of 256x256. Because this protocol

was repeated throughout the whole experiment, the k-space padding and apodization filter do not affect SNR calculation comparisons.

For baseline measurements, this protocol was repeated four times for the calculation of the average SNR_{mean} and SNR_{max} and their standard deviations.

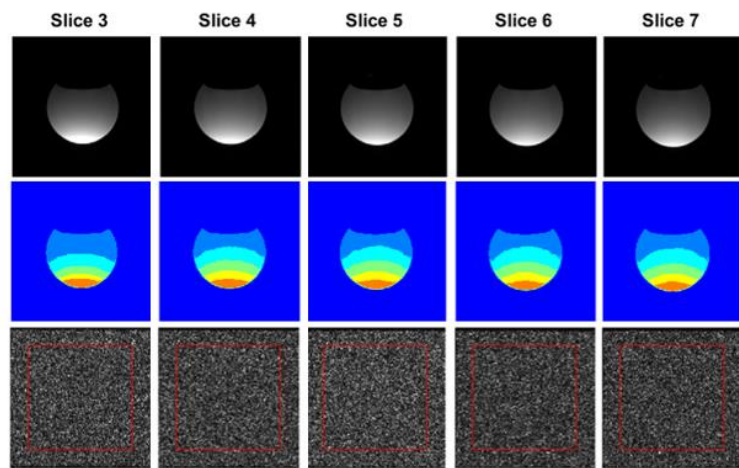


Figure 6: Row 1 depicts the signal image of slices 3, 4, 5, 6, and 7. Row 2 illustrates the 6 thresholds of intensity, with the dark blue representing the noise, and therefore not included in the signal measurements for SNR calculations. Row 3 demonstrates the noise image acquired with the 189x189 pixel noise ROI.

2.2 Method and protocol for evaluating complete disinfection of bacteria from a rigid endorectal coil

The efficacy of sterility testing of trophon® 2 as an HLD method for a rigid endorectal coil was investigated with respect to four bacteria: bacillus subtilis (EZ-Accu Shot™, Microbiologics, VWR, Lutterworth, United Kingdom, Cat. # 89504-665), pseudomonas

aeruginosa (Cat. # 89504-615), candida albicans (Cat. # 89504-371), and aspergillus brasiliensis (Cat. # 89504-073).

Each vial of freeze-dried bacteria was mixed with saline solution for reconstitution within a biological safety cabinet. Before introduction of bacteria to the endorectal coil, 1 mL all four bacteria were grown on separate tryptic soy agar plates. This step was done for two purposes: proving that the organisms used were capable of growing in the conditions in which the experiment was conducted, and second, providing a visual representation of the shape and color of each bacteria—thus allowing for differentiation between organism growth.

To test the effectiveness of trophon[®] 2 HLD to eradicate these organisms on the reusable endorectal coil, two experimental setups were established. For *Trial 1*, demonstrated in Figure 7 (row 1), the rigid endorectal coil was first disinfected with Clorox, a low-level disinfection (LLD) method. This was done to ensure no bacteria was present on the coil prior to experimentation. Once cleaned with Clorox, bacteria were placed on the coil. The coil was inoculated with 0.5 mL of each bacteria, each sample spanning about 1/4th of the coil. To confirm inoculation, two plates of agar made direct contact with the coil—the first plate (*plate a*) on the superior and the second plate (*plate b*) on the inferior section of the coil; therefore, each plate comes in contact with two bacteria samples. Following inoculation of the coil and exposure to control plates, one trophon[®] 2 HLD cycle was completed. Immediately after, two more media plates tested for the presence of bacteria, using the same two-plate method. This procedure was repeated three times to confirm complete, reproducible disinfection of the coil. Trial 2 involved all the same steps, except no LLD was used, meaning only trophon[®] 2 for HLD of the coil was tested (Figure 7, row 2).

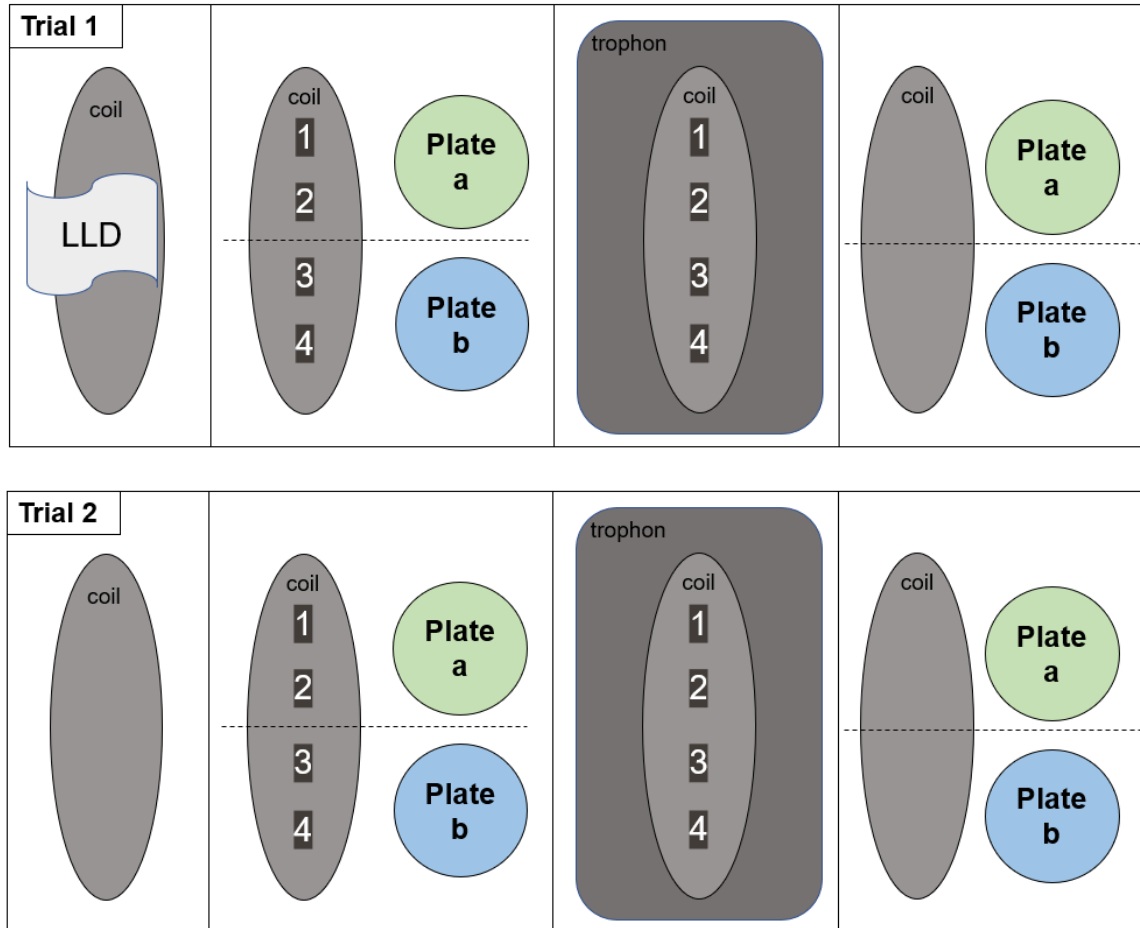


Figure 7: *Trial 1* involved LLD of the coil prior to inoculation with the use of a Clorox disinfection wipe. Then the coil was inoculated with the four bacteria on the coil at location 1, location 2, location 3, and location 4. After inoculation, two tryptic soy agar plates made direct contact with the coil to ensure successful inoculation. Plate a contacted the superior location of the coil, testing for bacteria at *Location 1* and 2, and *plate b* contacted the inferior section of the coil, testing for bacteria at *Location 3* and 4. Following this step, the coil received HLD in the trophon® 2. After HLD, the coil was tested with two more plates to test for the presence of bacteria. This experiment was repeated three times to test reproducibility.

Trial 2 involved all the same steps, except no LLD was used prior to inoculation—testing only the ability of the trophon® 2 for HLD of the rigid endorectal coil.

Because the endorectal coil extends beyond the recommended height within the chamber of the trophon® 2, indicated with an arrow in Figure 8, bacteria placement on the

coil was considered. Specifically, the disinfection of bacteria on the coil extending near and beyond embossed line were specified as *plate b*.



Figure 8: Arrow indicating the line that ultrasound transducers are recommended not to pass for disinfection; however, the rigid endorectal coil is longer. Locations labelled 1, 2, 3, and 4 represent the area for which each inoculated sample was placed. *Plate a* represents bacteria in locations 1 and 2, while *Plate b* represent locations 3 and 4. A syringe was used to inoculate the coil, and an L-spreader was used to spread the bacteria on the coil.

The placement of bacteria on the coil may affect the HLD ability of the trophon[®] 2. For this reason, the location of each bacteria was altered for each trial—specified in Table 4 and Table 5.

	Trial 1.1	Trial 1.2	Trial 1.3
Location 1	<i>Aspergillus brasiliensis</i>	<i>Aspergillus brasiliensis</i>	<i>Pseudomonas aeruginosa</i>
Location 2	<i>Candida albicans</i>	<i>Bacillus subtilis</i>	<i>Candida albicans</i>
Location 3	<i>Bacillus subtilis</i>	<i>Pseudomonas aeruginosa</i>	<i>Bacillus subtilis</i>
Location 4	<i>Pseudomonas aeruginosa</i>	<i>Candida albicans</i>	<i>Aspergillus brasiliensis</i>

Table 4: *Trial 1*—placement of each bacteria on the endorectal coil for trophon[®] 2 HLD cycle

After five days of incubation, each plate was assessed for bacterial growth, and the quantification of organism growth was based on the number of colony-forming-units (CFU).

	Trial 2.1	Trial 2.2	Trial 2.3
Location 1	Candida albicans	Pseudomonas aeruginosa	Aspergillus brasiliensis
Location 2	Aspergillus brasiliensis	Bacillus subtilis	Candida albicans
Location 3	Bacillus subtilis	Aspergillus brasiliensis	Pseudomonas aeruginosa
Location 4	Pseudomonas aeruginosa	Candida albicans	Bacillus subtilis

Table 5: *Trial 2*—placement of each bacteria on the endorectal coil for trophon® 2 HLD cycle

2.3 Method and protocol for assessing rigid endorectal coil properties with respect to trophon® 2 HLD

The rigid endorectal coil’s capacity to withstand trophon® 2 HLD with respect to physical and image performance properties was evaluated prior to, at consecutive sets of ten, and after one-hundred high level disinfection cycles.

2.3.1 Coil Baseline Assessment

For baseline coil performance, the QC methods and SNR calculations described in section 2.1.1 were used.

Physical property changes could affect patient comfort, patient safety, as well as coil performance. For example, after disinfection cycles, there may be a change in color, chipping of paint, or a break in surface coating or insulation that could compromise patient safety—thus pictures were acquired to document visual properties of the rigid endorectal coil.

To capture the coil in its entirety, pictures of the coil were obtained at twelve different angles. To maintain consistent imaging, parameters related to the coil, camera, and lighting were defined using tape to mark the location of the coil base as well as the imaging field-of-

view. The image angle and lighting were controlled by placing the camera on a stable lab-bench shelf, zooming to 3x, and turning on the bench light to illuminate all features of the coil. The front, back, and two sides of the coil, the neck of the coil, and the electronic casing were captured. After obtaining an image of each the six views shown in Figure 9, the coil was flipped and another set of images was taken—allowing for documentation of all sides of the coil.

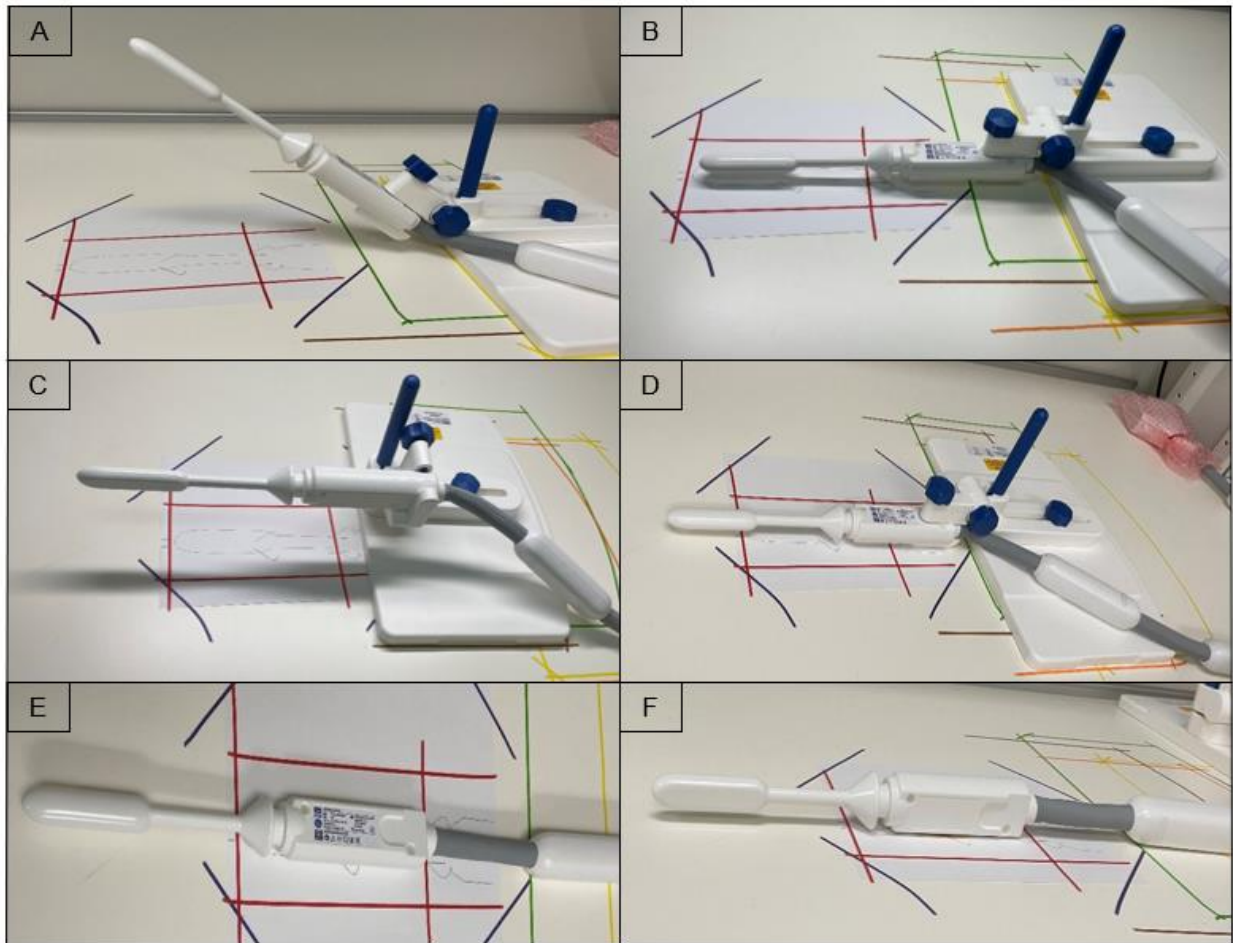


Figure 9: Image set-up for visual assessment of the coil. Red tape represents the field of view of each image; drawn on the paper are outlines of the coil to line up with. Tape colors green, purple, yellow, and orange specify the position of the coil's base depending on which angle of the coil is being imaged.

2.3.2 trophon[®] 2 Protocol

Once the baseline assessments were completed, the coil was exposed to a sequence of ten cycles of the trophon[®] 2 HLD process.

Prior to each run, using an infrared thermometer the temperature of the base of the coil's electronics, shown in Figure 10A, as well as the center of the coil's active region, displayed in Figure 10B, was measured and recorded. The coil was then placed within the chamber of the trophon[®] 2 for HLD.

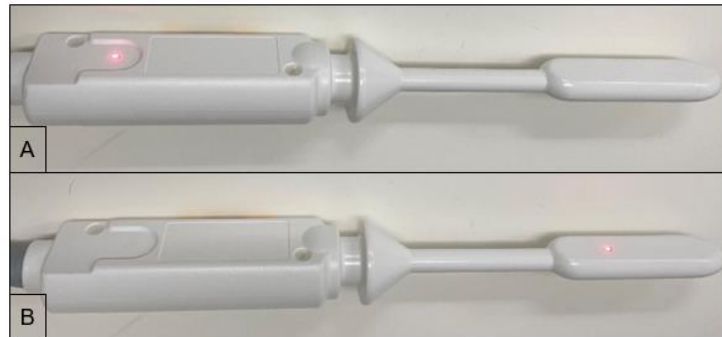


Figure 10: A) represents the location of temperature measured before and after each HLD cycle B) Location of temperature measured before each HLD cycle

There were two viable options of coil placement within the trophon[®] 2. Figure 11A places the coil as well as the electronic casing within the chamber of the trophon[®] 2. Figure 11B depicts the coil placed within the chamber of the trophon[®] 2, but the neck of the coil and the electronic casing would not receive HLD. If set-up A is implemented, the primary concern is that the electronic casing insulation is not sealed as well as the coil; if true, the electronics may be harmed if exposed the hydrogen peroxide treatment, thus hindering signal acquisition. However, in set-up B, the neck of the coil does not receive HLD—this region does make patient contact, and therefore requires HLD. Therefore, in this research, configuration A was selected.

When placing the coil within the chamber of the trophon[®] 2, it was ensured that no contact was made with the coil and the walls of the device. Subsequently a 7-minute HLD

cycle was started. Following each run, the temperature at the base of the electronic-section (Figure 10A) was measured and recorded a second time. Once the temperature of the coil (Figure 10A and Figure 10B) returned to room temperature, the protocol was repeated. Following the completion of ten cycles, the coil-baseline-assessment protocol (section 2.3.1) was repeated. However, for runs two through nine only a single set of MR images was acquired for SNR calculations.



Figure 11: Two options of rigid endorectal coil placement within the trophon® 2. Setup A requires the electronic casing to receive HLD—however, the electronic casing does not require HLD and may not be sealed as sufficiently as the coil and neck of the coil; setup B fails to provide HLD to the neck of the rigid endorectal coil. Because of this, this study uses setup A for HLD of the rigid endorectal coil

Chapter 3

Results

For clinical implementation of the trophon[®] 2 for HLD of rigid endorectal coils, it must be proven that HLD is reproducibly achieved. In addition, no decrease in the coil's SNR imaging abilities or change in physical properties should be observed with an increasing number of HLDs. This chapter presents the experimental data to assess the viability of trophon[®] 2 as a method of HLD for the rigid endorectal coil.

3.1 Experimental results from HLD of an inoculated rigid endorectal coil

Effective and reliable HLD of the rigid endorectal coil by means of trophon[®] 2 was assessed in three steps. First, confirmation of growth and physical appearance of each organism was evaluated. Figure 12 demonstrates the viability of bacterial growth in the experimental conditions provided as well as the physical appearance of each CFU; these plates are used as a reference in the following steps within specific aim 2.



Figure 12: Growth of aspergillus brasiliensis, bacillus subtilis, candida albicans, and pseudomonas aeruginosa for Trial 1 (row 1) and Trial 2 (row 2)—indicates the physical appearance of each organism as well as all organisms can grow in the experimental conditions defined

The second step involved inoculation of the coil, as well as the

investigation of which bacteria was successfully transferred to the coil; this was completed by making direct contact between the agar plates and the inoculated coil. The final inspection of bacterial growth was completed after an HLD cycle—accomplished by making direct contact of the agar plates with the coil.

For Trial 1.1 (Figure 13), inoculation *plate a* was expected to show bacterial growth from aspergillus brasiliensis and candida albicans; however, *plate a* showed successful inoculation of aspergillus brasiliensis, candida albicans and bacillus subtilis. *Plate a* had three different organisms due to inoculation on the coil not being exactly 1/4th for each bacterium. *Plate b* was expected to show growth of bacillus subtilis and pseudomonas aeruginosa and both bacteria inoculations were successful. After HLD, there was no presence of any bacteria on the coil.

Inoculation		Trial 1.1 inoculation:	Trial 1.1 Post HLD:	Post HLD
<i>Plate a</i> Expected	<i>Plate a</i> Results			<i>Plate a</i> Results
<ul style="list-style-type: none"> Aspergillus brasiliensis Candida albicans 	<ul style="list-style-type: none"> Aspergillus brasiliensis Candida albicans Bacillus subtilis 			--
<i>Plate b</i> Expected	<i>Plate b</i> Result			<i>Plate b</i> Result
<ul style="list-style-type: none"> Bacillus subtilis Pseudomonas aeruginosa 	<ul style="list-style-type: none"> Bacillus subtilis Pseudomonas aeruginosa 			--

Figure 13: For Trial 1.1, inoculation *plate a* showed successful inoculation of aspergillus brasiliensis, candida albicans and bacillus subtilis. *Plate b* presented growth from bacillus subtilis and pseudomonas aeruginosa. After HLD, there was no presence of any bacteria on the coil.

For Trial 1.2 (Figure 14), inoculation *plate a* was expected to show bacterial growth from *aspergillus brasiliensis* and *bacillus subtilis*; however, *plate a* only showed successful inoculation from *pseudomonas aeruginosa*. *Plate b* was expected to show growth from both *pseudomonas aeruginosa* and *candida albicans*, but neither inoculation was successful. After HLD, there was no presence of any bacteria on the coil.

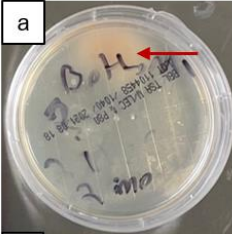
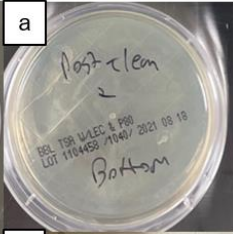
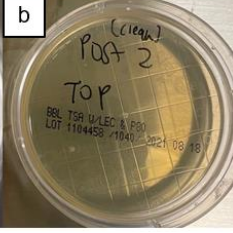
Inoculation		Trial 1.2 inoculation:	Trial 1.2 Post HLD:	Post HLD
<i>Plate a</i> Expected	<i>Plate a</i> Results			<i>Plate a</i> Results
<ul style="list-style-type: none"> Aspergillus brasiliensis Bacillus subtilis 	<ul style="list-style-type: none"> Pseudomonas aeruginosa 			--
<i>Plate b</i> Expected	<i>Plate b</i> Result			<i>Plate b</i> Result
<ul style="list-style-type: none"> Pseudomonas aeruginosa Candida albicans 	--			--

Figure 14: For Trial 1.2, inoculation *plate a* only showed successful inoculation of *pseudomonas aeruginosa*. Neither inoculation was successful for the inferior section of the coil, represented as *plate b*. After HLD, there was no presence of any bacteria on the coil.

For Trial 1.3 (Figure 15), inoculation *plate a* was expected to show bacterial growth from *pseudomonas aeruginosa* and *candida albicans*; however, there was only a successful inoculation of *pseudomonas aeruginosa*. *Plate b* was expected to show growth from *bacillus subtilis* and *aspergillus brasiliensis*, though neither inoculation was successful. After HLD, there was, again, no presence of any bacteria on the coil.

As Trial 1 progressed, there were fewer successful inoculations of the pre-HLD plates, and this is attributed to the use of the Clorox before each trial. For Trial 2, Clorox disinfection

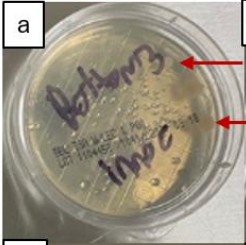
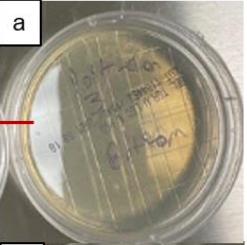
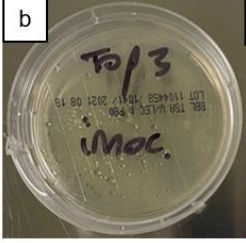
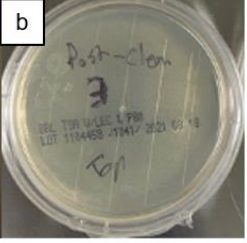
Inoculation		Trial 1.3 inoculation:	Trial 1.3 Post HLD:	Post HLD
<i>Plate a</i> Expected	<i>Plate a</i> Results			<i>Plate a</i> Results
<ul style="list-style-type: none"> • Pseudomonas aeruginosa • Candida albicans 	<ul style="list-style-type: none"> • Pseudomonas aeruginosa • Candida albicans 			--
<i>Plate b</i> Expected	<i>Plate b</i> Result			<i>Plate b</i> Result
<ul style="list-style-type: none"> • Bacillus subtilis • Aspergillus brasiliensis 	--			--

Figure 15: For Trial 1.3, inoculation *plate a* there was a successful inoculation of pseudomonas aeruginosa. Neither inoculation was successful for *plate b*. After HLD, there was no presence of any bacteria on the coil.

was not used, and only the trophon® 2 HLD abilities were tested.

For Trial 2.1 (Figure 16), inoculation *plate a* was expected to show bacterial growth from candida albicans and aspergillus brasiliensis; however, *plate a* showed successful inoculation of aspergillus brasiliensis and bacillus subtilis. *Plate b* was expected to show growth of bacillus subtilis and pseudomonas aeruginosa but only the pseudomonas aeruginosa was successful. After HLD, there was no presence of bacteria on *plate a*; however, *plate b* showed what appeared to be one CFU of candida albicans.

For Trial 2.2 (**Error! Reference source not found.**), inoculation *plate a* was expected to show bacterial growth from pseudomonas aeruginosa and bacillus subtilis; however, *plate a* showed successful inoculation of only pseudomonas aeruginosa. *Plate b* was expected to show growth of candida albicans and aspergillus brasiliensis but only the aspergillus brasiliensis was successful. After HLD, there was no presence of bacteria on *plate a*; however, *plate b* showed what appeared to be five CFU of candida albicans.

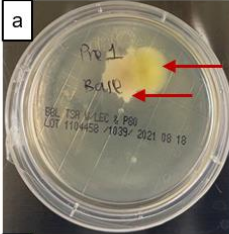
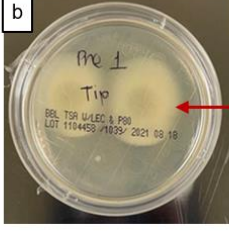
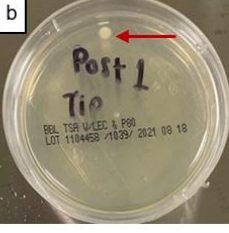
Inoculation		Trial 2.1 inoculation:	Trial 2.1 Post HLD:	Post HLD
<i>Plate a</i> Expected	<i>Plate a</i> Results			<i>Plate a</i> Results
<ul style="list-style-type: none"> Candida albicans Aspergillus brasiliensis 	<ul style="list-style-type: none"> Aspergillus brasiliensis Bacillus subtilis 			--
<i>Plate b</i> Expected	<i>Plate b</i> Result			<i>Plate b</i> Result
<ul style="list-style-type: none"> Bacillus subtilis Pseudomonas aeruginosa 	<ul style="list-style-type: none"> Pseudomonas aeruginosa 			<ul style="list-style-type: none"> Candida albicans

Figure 16: For Trial 2.1, inoculation *plate a* presented successful inoculation of aspergillus brasiliensis and bacillus subtilis. Pseudomonas aeruginosa was successfully inoculated, presented on *plate*. After HLD, there was no presence of bacteria on *plate a*; however, *plate b* showed what appeared to be one CFU of candida albicans.

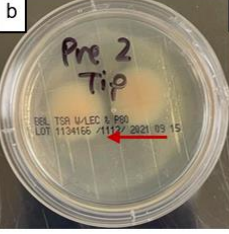
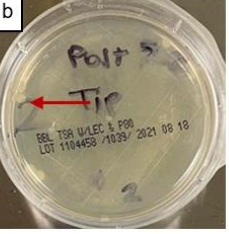
Inoculation		Trial 2.2 inoculation:	Trial 2.2 Post HLD:	Post HLD
<i>Plate a</i> Expected	<i>Plate a</i> Results			<i>Plate a</i> Results
<ul style="list-style-type: none"> Pseudomonas aeruginosa Bacillus subtilis 	<ul style="list-style-type: none"> Pseudomonas aeruginosa 			--
<i>Plate b</i> Expected	<i>Plate b</i> Result			<i>Plate b</i> Result
<ul style="list-style-type: none"> Aspergillus brasiliensis Candida albicans 	<ul style="list-style-type: none"> Aspergillus brasiliensis 			<ul style="list-style-type: none"> Candida albicans

Figure 17: For Trial 2.2, inoculation *plate a* showed successful inoculation of only pseudomonas aeruginosa. *Plate b* was showed that the aspergillus brasiliensis inoculation was successful. After HLD, there was no presence of bacteria on *plate a*; however, *plate b* showed what appeared to be five CFU of candida albicans.

For Trial 2.3 (Figure 18), inoculation *plate a* was expected to show bacterial growth from *aspergillus brasiliensis* and *candida albicans*; however, there was a successful inoculation of *pseudomonas aeruginosa* and *candida albicans*. *Plate b* was expected to show growth from *pseudomonas aeruginosa* and *bacillus subtilis*, though neither inoculation was successful. After HLD, there was no presence of any bacteria on the coil.

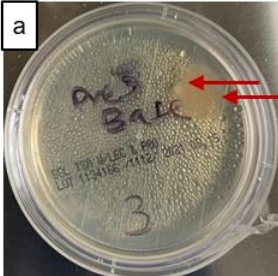
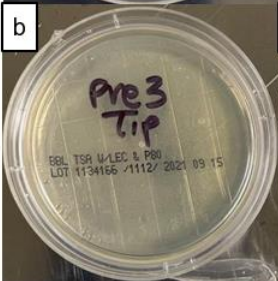
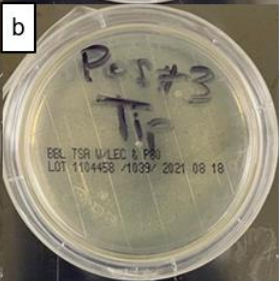
Inoculation		Trial 2.3 inoculation:	Trial 2.3 Post HLD:	Post HLD
<i>Plate a</i> Expected	<i>Plate a</i> Results			<i>Plate a</i> Results
<ul style="list-style-type: none"> Aspergillus brasiliensis Candida albicans 	<ul style="list-style-type: none"> Candida albicans Pseudomonas aeruginosa 			--
<i>Plate b</i> Expected	<i>Plate b</i> Result			<i>Plate b</i> Result
<ul style="list-style-type: none"> Pseudomonas aeruginosa Bacillus subtilis 	--			--

Figure 18: For Trial 2.3, inoculation *plate a*, there was a successful inoculation of *pseudomonas aeruginosa* and *candida albicans*. *Plate b* showed no growth from any bacteria. After HLD, there was no presence of any bacteria on the coil.

For the post-HLD plated from Trial 2.1 and 2.2, *plate b* showed growth of what appears to be *candida albicans*. A close-up of these growths is provided in Figure 19 for a closer inspection. Of note, the morphological presence of the *candida albicans* CFU on the control plate appear round and white. On the post-HLD plates shown in Figure 19, some of the CFUs have a yellow appearance. In addition, most of the surface area of the coil contacts the center of the agar plate—therefore, just as in the other inoculation plates—growth within the center of the plate is expected, rather than on the rim of the plates.

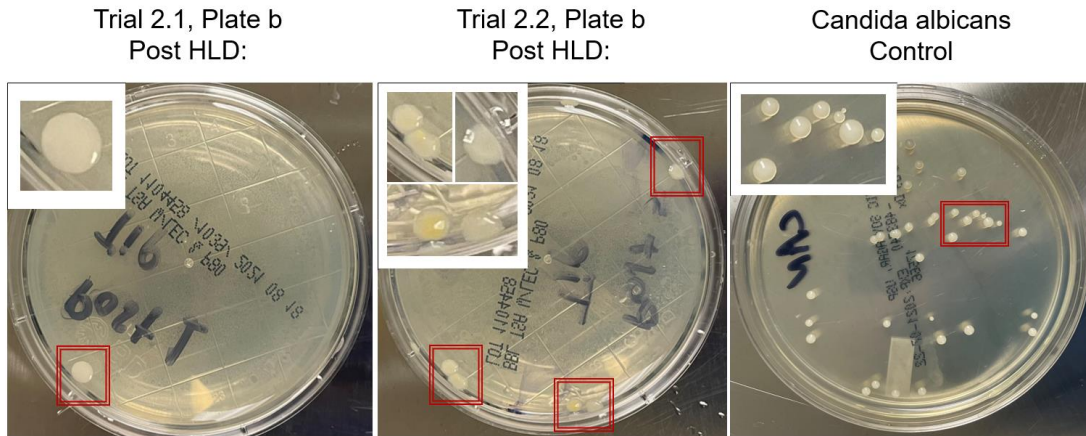


Figure 19: Close-up of the bacterial growth of post HLD *b-plates* from Trial 2.1 and 2.2 as well as the candida albicans control plate for reference.

3.2 Experimental results from assessing rigid endorectal coil properties with respect to trophon[®] 2 HLD

The aim of this section was to assess the pre- and post-HLD data acquired. First, the pre-HLD signal and SNR data was investigated. Because signal decreases with increasing distance from the receiver coil, the signal acquired is largest closest to the coil. As expected for the GE-EPI images, an artifact occurred due to the high gradient strength required for such a small field of view. With increasing number of HLD, if changes in SNR_{mean} , SNR_{max} , or artifact appearance occurred, this would infer that HLD by means of trophon[®] 2 decreased the coil's imaging ability.

From the baseline signal and noise images acquired for the SE and GRE pulse sequence, the average and standard deviation of SNR_{mean} and SNR_{max} was calculated for the water phantom and the saline phantom. The SNR after 100 HLD cycles is assessed and compared to this data.

The first aspect of interest was comparison of the baseline signal images acquired to the signal images acquired post 100 HLD cycles. Presented in Figure 20, there was no visual change in the signal measured.

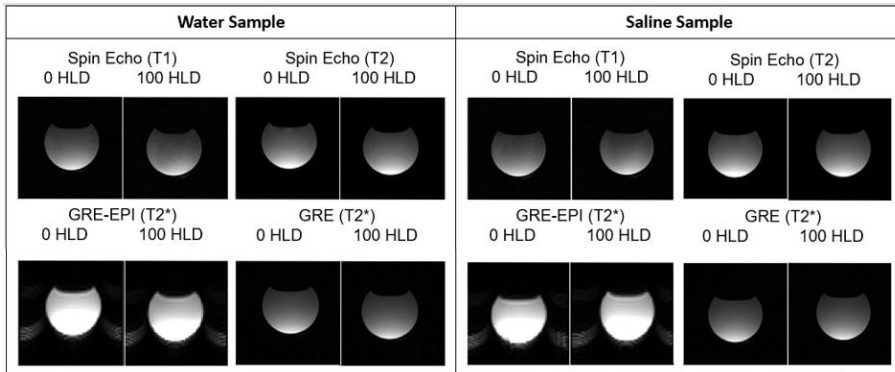


Figure 20: Signal images before and after 100 HLD cycles for Spin Echo (T_1 and T_2), GE-EPI (T_2^*), and GRE (T_2^*). No change in signal or artifacts is observed.

However, to determine if the strength of the signal changed with radial distance from the coil, the varying levels of signal, by means of Otsu's method—which was used to differentiate between the signal and noise for SNR data—is displayed and compared to the signal from the baseline images (Figure 21).

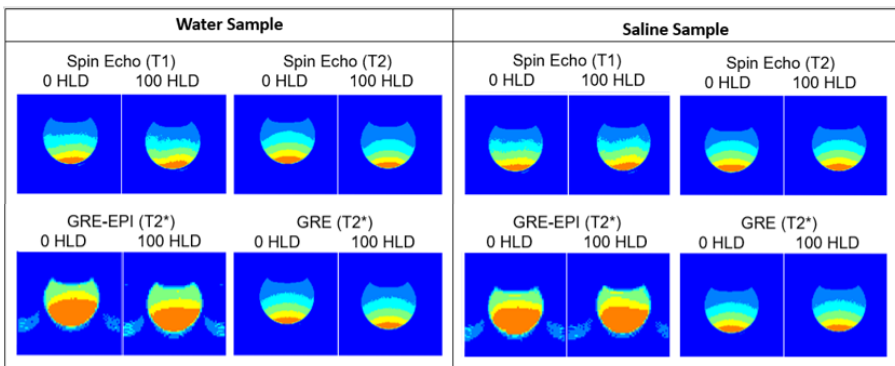


Figure 21: Comparison of threshold as calculated by Otsu's method for the water and the saline phantom

After evaluation of the visual images, the SNR data was investigated. Comparison of the QC data for pre- and post-100 HLD cycles are presented below for the water phantom (Figure 22) and the saline phantom (**Error! Reference source not found.**). All four pre-HLD SNR calculations were averaged and used to calculate the standard deviation, and same for the post-100 HLD. Of note, the 50 mL conical tube placement was at a slight angle, therefore, with increasing slice location along the MRI table, a decrease in SNR was observed.

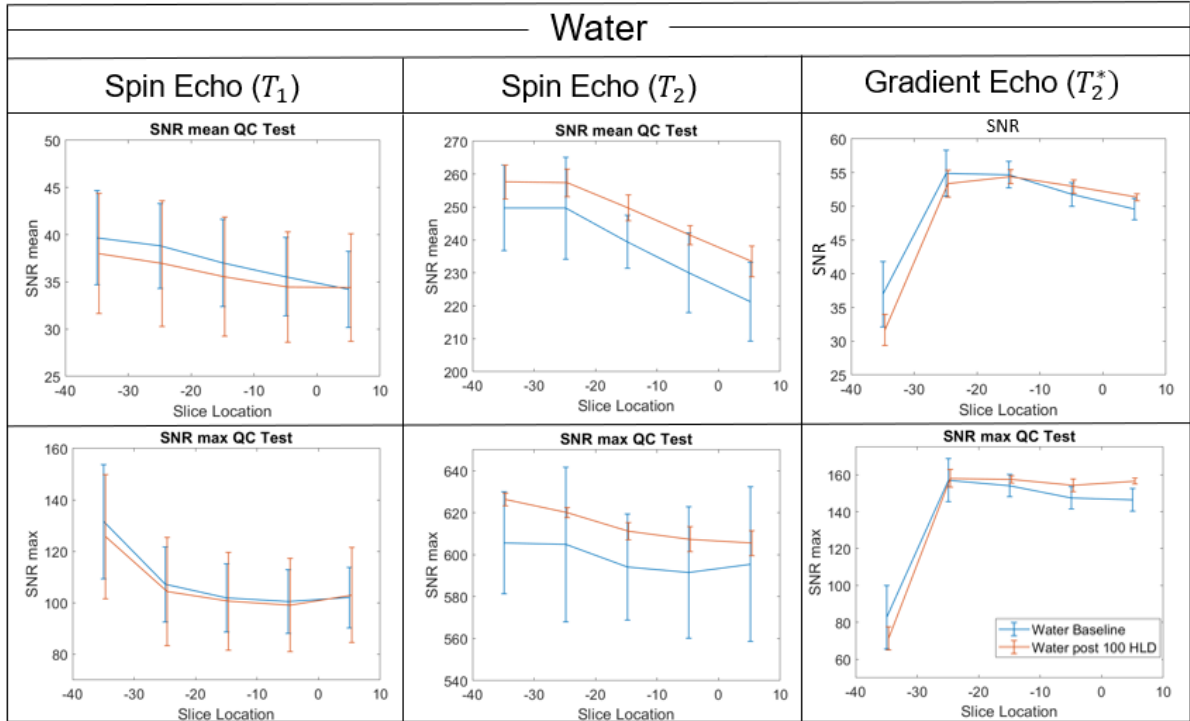


Figure 22: Comparison of the water phantom's baseline and post-100 HLD SNR_{mean} and SNR_{max} calculations.

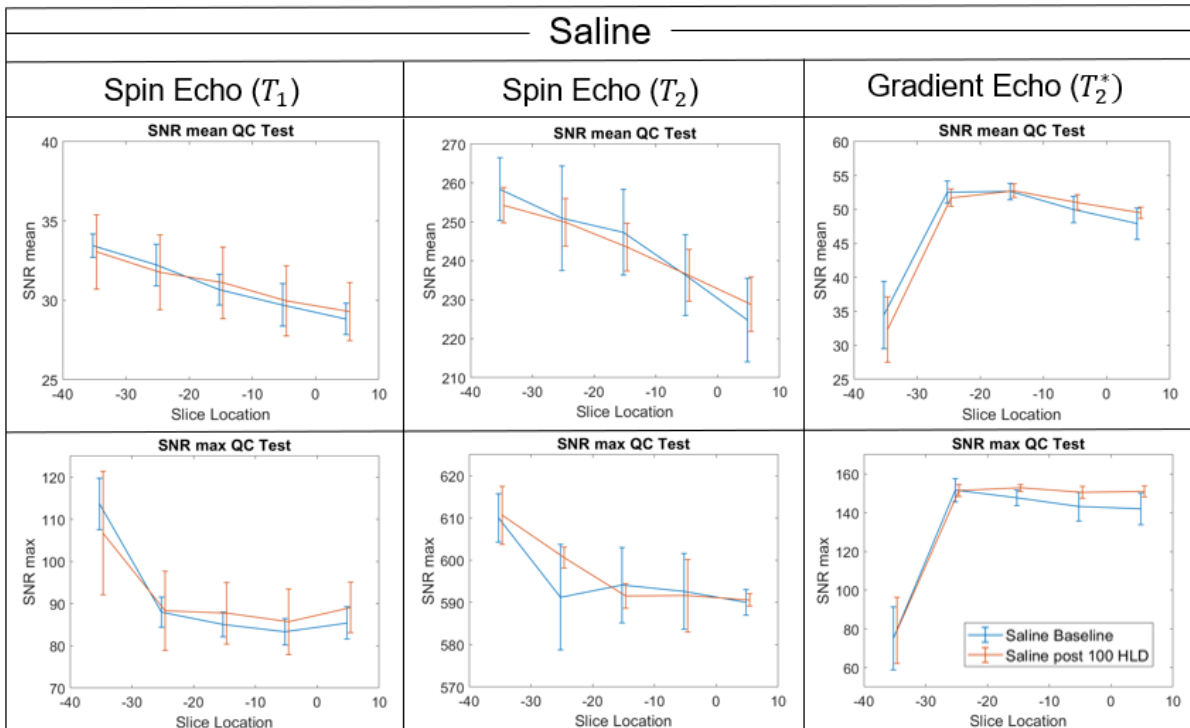


Figure 23: Comparison of the saline phantom's baseline and post-100 HLD SNR_{mean} and SNR_{max} data.

To compare the SNR_{mean} and SNR_{max} values of the 4 pre- and 4 post-100 HLD SNR data, a one-sided paired t-test was performed for slices 3, 4, 5, 6, and 7 (Table 6). This test is used to determine whether there is a significant difference between the average value of these sets of observations (before vs. after 100 cycles of HLD). Because there is concern that with increasing number of HLD cycles, there is a decrease in SNR, a one-sided paired t-test was utilized to test the hypothesis: SNR decreases with increasing number of HLD cycles. For each t-test, $p > 0.05$, therefore the null hypothesis—SNR does not decrease with increasing number of HLDs—cannot be rejected in any of these datasets.

Further assessment of the SNR_{mean} and SNR_{max} was evaluated with respect to the middle slice—slice 5—as a function of the cumulative number of HLD cycles. For both the water phantom (Figure 24) and saline phantom (Figure 25), an insignificant change in SNR occurs—as seen with each slope centered about 0 within the 95% confidence interval (

Saline		
<i>SNR_{mean}</i>		
	y-intercept	Number of HLD to decrease SNR by 10%
Spin Echo	30.08	215
Fast Spin Echo	237.3	168
Gradient Echo	50.97	364
<i>SNR_{max}</i>		
	y-intercept	Number of HLD to decrease SNR by 10%
Spin Echo	83.36	202
Fast Spin Echo	592.7	735

Table 7) and all p-values greater than 0.05, indicating that no statistically significant correlation was observed between coil SNR and cumulative exposure to the trophon® 2 HLD.

Additionally, in Table 9 and Table 7, the negative bound of the 95% confidence interval for the slope of the regression was used to estimate the

number of trophon® 2 HLD cycles that would be necessary to cause a 10% decrease SNR.

For the Spin Echo pulse sequences acquired on the water phantom, fewer than 100 HLD cycles was determined to decrease the SNR by more than 10%. However, due to inconsistent transmit gain calibration values (found in Appendix A) for the water phantom SE sequences, there was an increased variance seen in SNR data, and a wider 95% confidence interval for the slope of the regression. Because this variation is associated with transmit calibration and not random variations in our SNR data, we do not believe this to be an accurate estimate of the effects of HLD. Estimates from the regression of all other datasets indicate that at least 168 cycles would be needed to decrease the SNR by 10%.

Gradient Echo	144.8	559
---------------	-------	-----

Table 7: Estimated number of HLD cycles required to reduce the SNR by 10% of the original value—using the lowest value of slope in the 95% confidence level define in **Error! Not a valid bookmark self-reference.** with respect to the saline phantom.

Pulse Sequence	Slice 3	Slice 4	Slice 5	Slice 6	Slice 7
Water SNR_{mean}					
SE (T_1)	✓ $P = 0.3592$	✓ $P = 0.3590$	✓ $P = 0.3873$	✓ $P = 0.4160$	✓ $P = 0.5082$
SE (T_2)	✓ $P = 0.8319$	✓ $P = 0.8595$	✓ $P = 0.9896$	✓ $P = 0.9537$	✓ $P = 0.9697$
GRE (T_2^*)	✓ $P = 0.0834$	✓ $P = 0.2359$	✓ $P = 0.4321$	✓ $P = 0.8279$	✓ $P = 0.9416$
Water SNR_{max}					

SE (T_1)	✓ $P = 0.3847$	✓ $P = 0.4291$	✓ $P = 0.4661$	✓ $P = 0.4602$	✓ $P = 0.5290$
SE (T_2)	✓ $P = 0.8933$	✓ $P = 0.7615$	✓ $P = 0.8673$	✓ $P = 0.7861$	✓ $P = 0.6982$
GRE (T_2^*)	✓ $P = 0.1460$	✓ $P = 0.5564$	✓ $P = 0.8262$	✓ $P = 0.9328$	✓ $P = 0.9785$
Saline SNR_{mean}					
SE (T_1)	✓ $P = 0.3835$	✓ $P = 0.4360$	✓ $P = 0.6099$	✓ $P = 0.5584$	✓ $P = 0.6171$
SE (T_2)	✓ $P = 0.3082$	✓ $P = 0.4558$	✓ $P = 0.3304$	✓ $P = 0.4876$	✓ $P = 0.6586$
GRE (T_2^*)	✓ $P = 0.3490$	✓ $P = 0.2866$	✓ $P = 0.6749$	✓ $P = 0.8300$	✓ $P = 0.8694$
Saline SNR_{max}					
SE (T_1)	✓ $P = 0.2572$	✓ $P = 0.5178$	✓ $P = 0.6487$	✓ $P = 0.6533$	✓ $P = 0.7631$
SE (T_2)	✓ $P = 0.5587$	✓ $P = 0.8512$	✓ $P = 0.3037$	✓ $P = 0.4505$	✓ $P = 0.6736$
GRE (T_2^*)	✓ $P = 0.6037$	✓ $P = 0.4841$	✓ $P = 0.9829$	✓ $P = 0.9329$	✓ $P = 0.9339$

Table 6: One-sided paired t-test for each slice, comparing the 4 pre-HLD SNR data to the post-100 HLD data. The check represents the null hypothesis could not be rejected; the p-value is > 0.05 for each test.

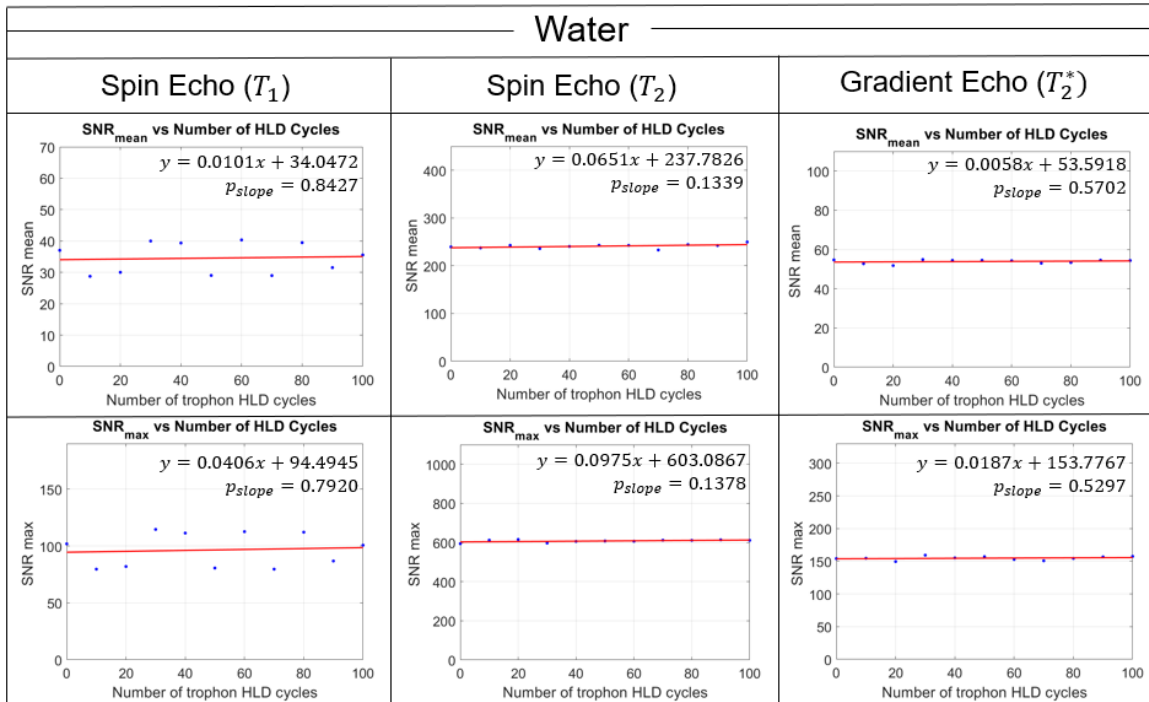


Figure 24: Slice 5 of the water phantom, SNR_{mean} and SNR_{max} plots versus HLD cycle number. The slope of each linear regression is centered about zero at the 95% confidence level, with a p-value > 0.05.

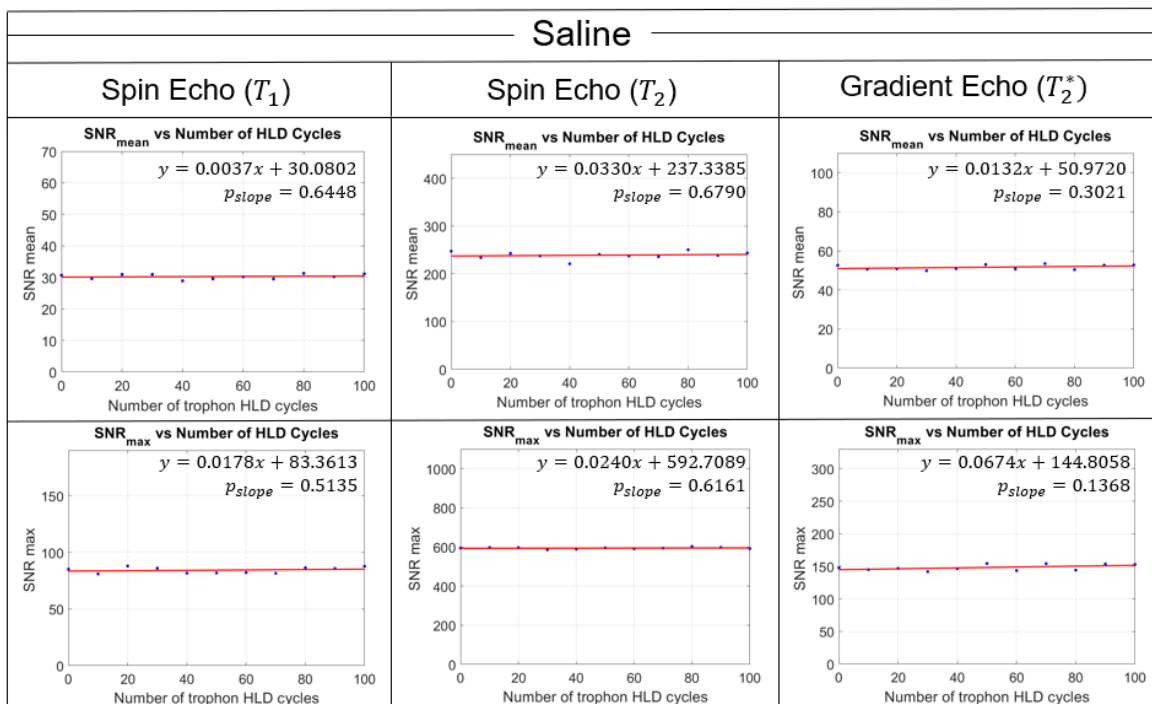


Figure 25: Slice 5 of the saline phantom, SNR_{mean} and SNR_{max} plots versus HLD cycle number. The slope of each linear regression is centered about zero at the 95% confidence level, with a p-value > 0.05.

	Water		Saline	
	<i>SNR_{mean}</i>		<i>SNR_{mean}</i>	
	<i>m₋</i>	<i>m₊</i>	<i>m₋</i>	<i>m₊</i>
Spin Echo	-0.1017	0.1219	-0.014	0.0215
Fast Spin Echo	-0.0243	0.1544	-0.1416	0.2076
Gradient Echo	-0.0165	0.02815	-0.014	0.04038
	<i>SNR_{max}</i>		<i>SNR_{max}</i>	
	<i>m₋</i>	<i>m₊</i>	<i>m₋</i>	<i>m₊</i>
	Spin Echo	-0.2971	0.3783	-0.0413
Fast Spin Echo	-0.0379	0.233	-0.0807	0.1288
Gradient Echo	-0.0459	0.08325	-0.0259	0.1607

	Saline	
	<i>SNR_{mean}</i>	
	y-intercept	Number of HLD to decrease SNR by 10%
Spin Echo	30.08	215
Fast Spin Echo	237.3	168
Gradient Echo	50.97	364
	<i>SNR_{max}</i>	
	y-intercept	Number of HLD to decrease SNR by 10%
	Spin Echo	83.36
Fast Spin Echo	592.7	735
Gradient Echo	144.8	559

Table 7: Estimated number of HLD cycles required to reduce the SNR by 10% of the original value—using the lowest value of slope in the 95% confidence level define in **Error!**

Table 8: 95% confidence interval of slopes in Figure 24 and Figure 25

Not a valid bookmark self-reference. with respect to the saline phantom.

Water		
<i>SNR_{mean}</i>		
	y-intercept	Number of HLD to decrease SNR by 10%
Spin Echo	34.0472	34
Fast Spin Echo	237.8	979
Gradient Echo	53.59	324
<i>SNR_{max}</i>		
	y-intercept	Number of HLD to decrease SNR by 10%
Spin Echo	94.49	32
Fast Spin Echo	603.1	1591
Gradient Echo	153.8	335

Table 9: Estimated number of HLD cycles required to reduce the SNR by 10% of the original value—using the lowest value of slope in the 95% confidence level define in

Saline		
<i>SNR_{mean}</i>		
	y-intercept	Number of HLD to decrease SNR by 10%
Spin Echo	30.08	215

Fast Spin Echo	237.3	168
Gradient Echo	50.97	364
	<i>SNR_{max}</i>	
	y-intercept	Number of HLD to decrease SNR by 10%
Spin Echo	83.36	202
Fast Spin Echo	592.7	735
Gradient Echo	144.8	559

Table 7: Estimated number of HLD cycles required to reduce the SNR by 10% of the original value—using the lowest value of slope in the 95% confidence level define in **Error!** **Not a valid bookmark self-reference.** with respect to the saline phantom.

In addition to evaluating SNR, physical properties were also documented with increasing cycles of HLD.

The temperature of the electronic casing and center of the coil (location shown in Figure 10A and Figure 10B) were measured before each run, and the electronic casing's temperature (position shown in Figure 10A) was measured after each run. To simulate clinical use, before subsequent HLDs, the temperature of the coil was left untouched until the temperature returned to baseline. The results are present in Table 10, Table 11, and Table 12.

Table 8 with respect to the water phantom.

Coil Electronics—Pre HLD												
HLD Cycles	Temperature ± 0.95 °C										μ	σ
1 - 10	22.7	22.6	22.7	21.8	21.5	22.9	22.0	22.0	21.7	22.2	22.2	0.14
11 - 20	23.8	23.7	23.5	23.4	23.3	23.3	23.8	22.7	22.6	22.8	23.3	0.13
21 - 30	23.7	22.1	23.4	23.4	23.1	23.0	23.4	23.1	21.9	21.7	22.9	0.13
31 - 40	23.7	23.1	22.3	23.7	23.1	23.0	22.5	22.6	22.7	23.3	23.0	0.13
41 - 50	23.8	23.5	23.4	22.3	22.6	23.5	23.0	23.3	22.9	22.8	23.1	0.13

51 - 60	23.7	23.6	22.7	22.8	22.9	22.7	23.3	22.8	22.8	23.3	23.1	0.13
61 - 70	23.8	23.1	23.6	22.7	22.8	23.2	22.9	23.2	23.3	22.5	23.1	0.13
71 - 80	23.9	23.4	23.1	23.0	23.2	23.1	23.1	23.1	23.3	23.2	23.2	0.13
81 - 90	23.7	23.7	22.8	23.1	23.1	23.2	22.9	23.1	23.2	23.3	23.2	0.13
91 - 100	23.6	23.8	23.1	23.2	23.2	22.9	23.3	23.2	22.9	23.4	23.3	0.13

Table 10: Pre-HLD temperature of the electronic casing

Coil—Pre HLD												
HLD Cycles	Temperature ± 0.95 °C										μ	σ
1 - 10	22.7	22.6	22.9	22.2	22.1	22.9	21.7	22.6	22.2	22.0	22.4	0.13
11 - 20	22.7	22.6	22.7	22.8	22.6	22.8	22.3	22.5	22.3	22.4	22.6	0.13
21 - 30	22.7	22.1	22.5	22.8	22.7	22.8	22.5	22.4	21.9	21.7	22.4	0.13
31 - 40	22.8	22.3	22.3	22.7	22.7	22.7	22.0	22.4	22.3	22.9	22.5	0.13
41 - 50	22.7	22.5	22.4	22.4	22.4	22.6	22.7	22.6	22.3	22.7	22.5	0.13
51 - 60	22.8	22.5	22.4	22.5	22.4	22.3	22.7	22.4	22.5	22.4	22.5	0.13

61 - 70	22.9	22.7	22.6	22.6	22.5	22.1	22.6	22.4	22.5	22.5	22.5	0.13
71 - 80	22.7	22.4	22.7	22.7	22.6	22.3	22.5	22.5	22.6	22.5	22.6	0.13
81 - 90	22.7	22.6	22.7	22.7	22.6	22.6	22.5	22.4	22.5	22.7	22.6	0.13
91 - 100	22.8	22.6	22.5	22.7	22.5	22.6	22.5	22.5	22.6	22.5	22.6	0.13

Table 11: Pre-HLD temperature of the coil

Coil Electronics—Post HLD												
HLD Cycles	Temperature ± 0.95 °C										μ	σ
1 - 10	49.3	48.9	48.7	44.6	44.4	43.0	47.1	42.1	42.7	42.4	45.3	0.07
11 - 20	49.3	47.1	48.1	46.5	44.1	47.7	47.5	45.9	41.9	44.4	46.3	0.07
21 - 30	49.7	42.3	44.5	46.7	43.2	43.2	44.1	43.4	42.1	43.5	44.3	0.07
31 - 40	46.1	43.1	42.7	47.1	43.3	46.4	40.5	41.2	43.8	43.7	43.8	0.07
41 - 50	49.4	44.7	45.8	47.2	43.1	45.7	46.6	42.5	45.7	47.8	45.9	0.07
51 - 60	51.7	48.3	44.2	46.4	43.1	42.8	44.2	42.9	44.2	46.1	45.4	0.07

61 - 70	51.7	45.4	46.1	44.8	45.1	45.6	44.8	42.6	43.7	44.9	45.5	0.07
71 - 80	48.3	48.3	47.7	44.8	44.0	45.4	43.4	43.5	44.0	44.6	45.4	0.07
81 - 90	47.7	44.3	45.7	44.2	42.8	46.0	43.1	43.8	44.4	44.6	44.7	0.07
91 - 100	48.1	48.5	46.9	44.0	45.7	45.7	44.2	43.6	43.2	43.7	45.4	0.07

Table 12: Post-HLD temperature of the electronic casing

Visual images of the coil before introduction to HLD and after 100 cycles of HLD were documented. The coil post-100 HLD shows no change in color or shape when compared to the pre-HLD images (Figure 26). Similarly, the post 100 HLD neck of the coil images also present no obvious change in physical appearance when compared to the pre-HLD images (Figure 27).

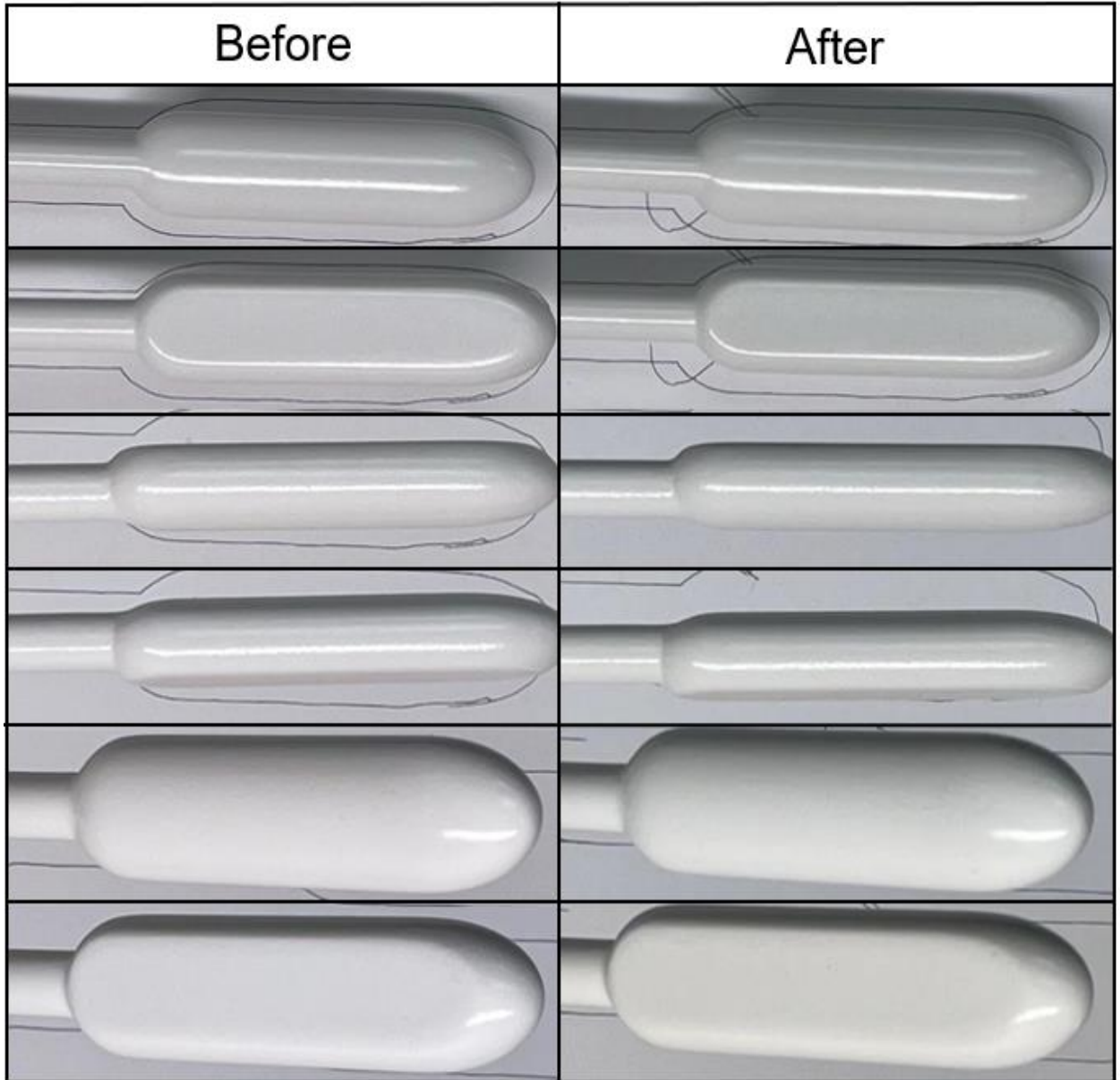


Figure 26: Coil images pre and post 100 trophon® 2 HLD cycles

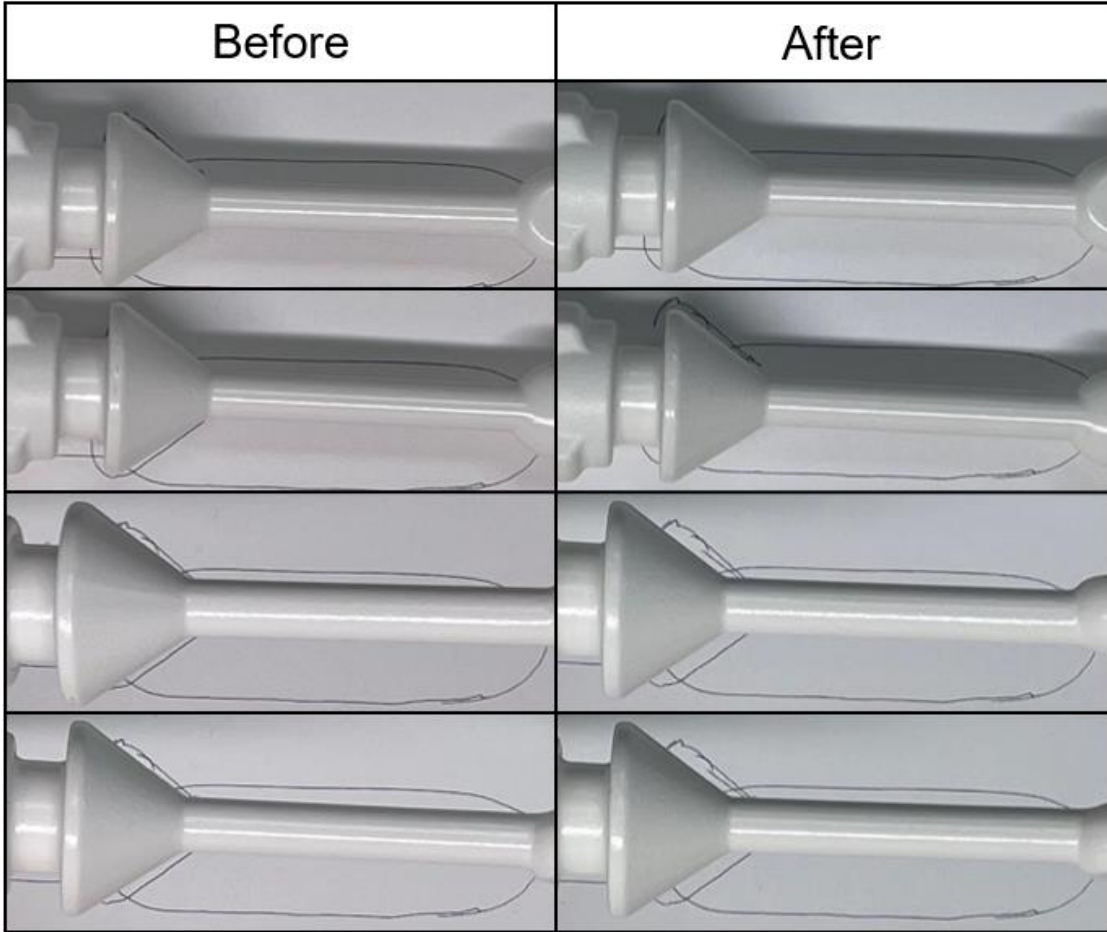


Figure 27: Images of the neck of the coil pre and post 100 trophon[®] 2 HLD cycles

On closer inspection, a small bubble at the tip of the coil formed after 70 HLD runs (**Error! Reference source not found.**).



Figure 28: Small bubble formed on the tip of the rigid endorectal coil post 70 HLD cycles in the trophon[®] 2

Also of note, imaged in **Error! Reference source not found.**, on the base of the coil's neck is chip in paint; however, this chip of paint was present before introduction to the trophon[®] 2 (Figure 30).



Figure 29: Chip on the base of the neck—present pre and post 100 HLD cycles.

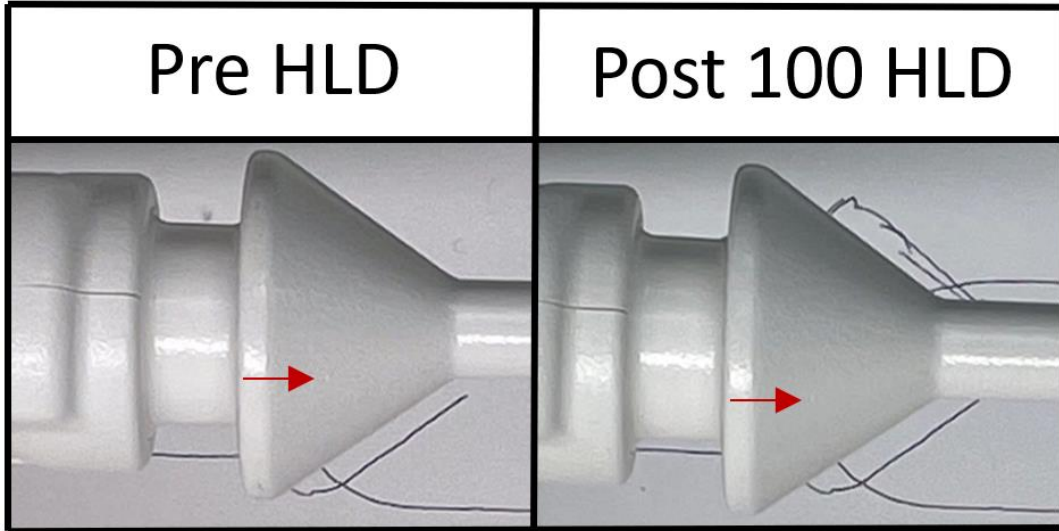


Figure 30: Chip on the base of the neck of the coil, present before and after 100 HLD cycles

In addition, physical changes of the electronic casing were assessed; the pre and post-100 HLD images of the electronic casing are presented in Figure 31.



Figure 31: Images of the electronics region of the coil pre and post 100 trophon® 2 HLD cycles

On the casing of the electronics, formation of bubbles (Figure 32A and Figure 32B) and chips in paint were observed (Figure 32C), as well as bubble formation under the informational stickers (Figure 32B).

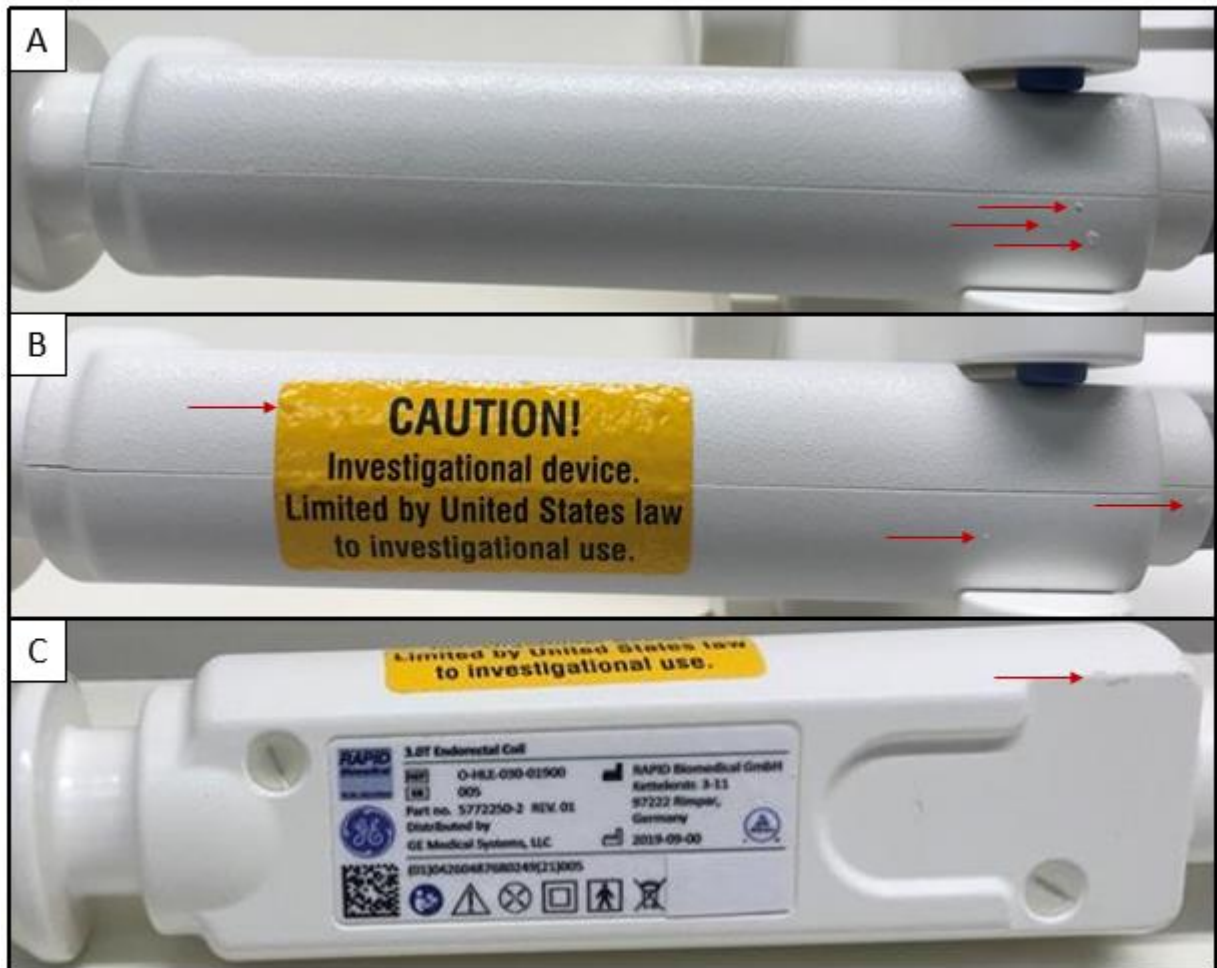


Figure 32: A) Formation of bubbles from the paint on the casing of the electronics B) formation of bubbles on the paint of the casing of the electronics as well as under the caution sticker C) chips in paint on the electronic casing

Chapter 4

Discussion

4.1 Impact of trophon[®] 2 HLD on a reusable endorectal MRI coil

Rigid endorectal coils are commercially available but are not used in practice in clinical settings. A method for providing complete disinfection of the coil that does not degrade SNR is required for routine clinical implementation.

Addressed in section 2.2 was the HLD effectiveness of a rigid endorectal coil by means of trophon[®] 2. Post HLD agar plates showed complete bacterial disinfection, except for trials 2.1 and 2.2; these trials showed CFU on the post-HLD *b-plates* with a similar appearance as the candida albicans control plate. After examining the appearance of the post-HLD plates to the candida albicans control (as shown in Figure 19), there were four indications signifying the CFUs are contaminants and not candida albicans resulting from direct exposure of the coil to the test plates. First, the circular shape is well defined for the control plate but not for the post-HLD *b plate* from Trial 2.2. Second, some of the colonies presented a yellow-tint—which is not seen on the control plate. Third, growth of bacteria only was presented on the edges of the agar plate—suggesting contamination occurred when handling the plates. Moreover, most of the surface area of the agar plate in contact with the coil was at the center—as seen in the pre-HLD plates. And finally, there was no presence of candida albicans on the pre-HLD *b-plates* for trial 2.1 and 2.2—therefore, the post-HLD *b-plates* would not present growth of candida post-HLD.

Thus, it is concluded that the trophon[®] 2 showed complete elimination of bacillus subtilis, pseudomonas aeruginosa, candida albicans, and aspergillus brasiliensis.

In section 2.1 the protocol, method, hardware setup, initial MRI images, and SNR calculations were defined. The main objective of this section was to establish infrastructure to ensure consistent and reproducible position of the coil with respect to the phantom and the bore of the MRI.

Presented in section 2.3 were the signal images of pre- post-100 HLD cycles (Figure 20); the pre-HLD signal images of the SE and GRE pulse sequences, for both the water and saline phantom, there were no observable artifacts. However, as expected, the GE-EPI images presented an artifact; this artifact occurs due to the strength of gradient required for such a small field of view. Then observing the post-HLD signal images, even after all 100 HLDs, no qualitative differences were detected—not even a visible difference in the artifact present in the GE-EPI image. Therefore, 100 trophon[®] 2 HLD cycles of the rigid endorectal coil did not disrupt the qualitative imaging properties of the MR image.

Quantitative measurements were also examined. The SNR_{mean} and SNR_{max} , for both the water and saline phantom were calculated. Presented in Figure 22 and **Error!** **Reference source not found.** are the comparison of the baseline SNR with the post-100 HLD SNR. By comparing the pre- and post-HLD data with a one-sided paired t-test, it was determined that the null hypothesis—SNR does not decrease with increasing number of HLD cycles—cannot be rejected.

Furthermore, the SNR data as a function of the number of HLDs was assessed. In Figure 24 and Figure 25, it can be observed that the negligible slope of SNR as a function of HLDs, suggests no degradation of SNR due to HLD. In addition to the negligible slope, the p-value of each slope was above 0.05; therefore, the null hypothesis—SNR does not decrease with increasing number of HLD cycles—cannot be rejected. From estimating the number of HLD cycles to decrease the measured SNR by 10%, it was determined that more

than 100 HLD cycles of the coil would be required for all sequences except for SE of the water phantom; however, this can be explained by variations in transmit gain that were found during the automatic pre-scan. If the transmit gain was not set to produce a 90-degree excitation, the maximum signal is not obtained and therefore a smaller SNR is measured. As observed in the SNR data from SE, variation in the transmit gain values produced variations in SNR calculations. Therefore, these variations are not ideal for estimating the effects of HLD on the rigid endorectal coil. However, all other transmit gain values were consistent. For example, for Fast Spin Echo of the saline phantom, it is estimated that 168 cycles would be needed, and for the water phantom, 980 HLD cycles would be required to decrease the SNR_{mean} by 10%.

Looking at the physical images of the endorectal coil, there was no significant change in physical appearance for the coil and the neck of the coil. However, on closer inspection, a small bubble formed on the tip of the coil after 70 HLD runs. Although this bubble formed, it was proven that the null hypothesis could not be rejected, and therefore. However patient safety with regards to this deformity still needs to be assessed.

Although the casing of the electronics presented physical changes, they did not affect the imaging properties of the coil. In addition, the electronic region will not come in contact with the patient and therefore does not need HLD.

4.2 Future Directions

A trophon[®] 2 has been shown to successfully achieve HLD on a rigid, reusable endorectal MRI coil without compromising sensitivity across at least 100 HLD cycles. However, the rigid endorectal coil is not yet ready to be implemented in the clinic for MRI coil HLD.

To further test the ability of trophon[®] 2 for HLD, disinfection of staphylococcus aureus from the coil should be tested—this was a biosafety level 2 organisms recommended by USP-NF for sterility testing.

Before experimentation with staphylococcus aureus, it is ideal the rigid endorectal coil be re-designed. In its current state, either the preamp box must go in the trophon[®] 2, which causes the coil to extend beyond the recommended length—the arrangement used in this study—or only the coil, omitting the neck of the coil, receives HLD. Preferably, the preamplifier box would sit outside of the trophon[®] 2 chamber, while both the neck and the coil receive HLD. This would decrease concerns of damage to the more sensitive electronics—although proven not to be an issue for up to 100 HLD cycles—and patient safety due to chipping of paint or damage to the coil structure, which is not sealed as tightly in this area.

As observed, after 70 cycles of HLD, a small bubble formed at the top of the coil. Although the paint was still intact and had no effect on the SNR measured, observation of bubble formation should be evaluated once a re-designed rigid endorectal coil has been developed. At present, the base of the chamber is closer to the coil than intended. It is possible this non-ideal condition—such as increased heat due to close-proximity of the coil to the base of the chamber—caused the formation of a bubble. However, the coil will be sent back to the manufacturer to determine if these flaws present a safety concern. If they do, a different surface coating for the coil and the neck of the coil—what will come in direct contact with the patient—will be evaluated.

Implementation of trophon[®] 2 as a process of HLD may allow for wider adoption of a rigid endorectal coil in the clinic. Consequently, higher SNR images may be acquired and even an increase in patient comfort. In addition, a receiver coil for 13C-based MRI imaging

for use in a clinic becomes more feasible, potentially changing the way prostate cancer is detected and assessed for therapy effectiveness.

For example, WW patients receive invasive diagnostic testing to determine if the tumor has increased in aggressiveness. With ^{13}C -based MRI, noninvasive diagnostic imaging can be acquired and samples the entire tumor. In addition, for patients receiving other forms of therapy, a ^{13}C -based MRI can be used to assess treatment efficacy before the end of treatment; this is because increases in tumor metabolic properties can be observed before changes in tumor size can be detected.

Appendix A

Automatic Pre-Scan Values

R1 – excitation pulse

R2 – refocusing pulse

TG – transmission gain

CF – center frequency

Water Sample	Pre HLD #1	Pre HLD #2	Pre HLD #3	Pre HLD #4	Post 100 HLD #1	Post 100 HLD #2	Post 100 HLD #3	Post 100 HLD #4
SE (T1)								
R1	13	13	13	13	13	13	13	13
R2	30	29	30	30	30	30	30	30
TG	142	129	143	142	123	143	127	143
CF	127746988	127747151	127746983	127746984	127746976	127746965	127746956	127746960
SE (T2)								
R1	13	13	13	13	13	13	13	13
R2	30	30	30	30	30	30	30	30
TG	119	118	121	119	119	121	123	123
CF	127746969	127746968	127746960	127746969	127746976	127746964	127746956	127746960
GE-EPI (T2*)								
R1	13	13	13	13	13	13	13	13
R2	15	15	15	15	30	15	15	15
TG	118	121	122	121	129	122	122	124
CF	127746981	127746968	127746983	127746946	127746976	127746965	127746956	127746960
GRE (T2*)								
R1	13	13	13	13	13	13	13	13
R2	15	15	15	15	15	15	15	15
TG	119	122	122	117	119	120	122	123
CF	127746981	127746968	127746983	127746972	127746976	127746972	127746956	127746960

Water Sample	Pre HLD	Post 10 HLD	Post 20 HLD	Post 30 HLD	Post 40 HLD	Post 50 HLD	Post 60 HLD	Post 70 HLD	Post 80 HLD	Post 90 HLD	Post 100 HLD
SE (T1)											
R1	13	13	13	13	13	13	13	13	13	13	13
R2	30	30	30	30	30	30	30	30	30	30	30
TG	142	124	127	142	143	124	144	124	141	127	123
CF	127746984	127746968	127746960	127746969	127747026	127746997	127746970	127746973	127746981	127746969	127746976
SE (T2)											
R1	13	13	13	13	13	13	13	13	13	13	13
R2	30	30	30	30	30	30	30	30	30	30	30
TG	119	119	122	118	119	121	121	118	121	119	119
CF	127746969	127746968	127746960	127746969	127747026	127746997	127746963	127746973	127746981	127746969	127746976
GE-EPI (T2*)											
R1	13	13	13	13	13	13	13	13	13	13	13
R2	15	15	15	15	15	15	15	15	15	15	30
TG	121	120	122	119	118	121	118	118	119	120	129
CF	127746946	127746968	127746960	127746969	127747026	127746997	127746970	127746973	127746981	127746969	127746976
GRE (T2*)											
R1	13	13	13	13	13	13	13	13	13	13	13
R2	15	15	15	15	15	15	15	15	15	15	15
TG	117	120	122	118	118	119	119	121	121	119	119
CF	127746972	127746968	127746960	127746969	127747026	127746997	127746970	127746973	127746981	127746969	127746976

Saline Sample	Pre HLD #1	Pre HLD #2	Pre HLD #3	Pre HLD #4	Post 100 HLD #1	Post 100 HLD #2	Post 100 HLD #3	Post 100 HLD #4
SE (T1)								
R1	13	13	13	13	13	13	13	13
R2	30	30	30	30	30	30	30	30
TG	125	125	128	126	124	125	127	132
CF	127746978	127746972	127746969	127746941	127746968	127746964	127746952	127746956
SE (T2)								
R1	13	13	13	13	13	13	13	13
R2	30	30	30	30	30	30	30	30
TG	120	122	126	118	120	120	122	125
CF	127746978	127746972	127746969	127736948	127746968	127746964	127746952	127746963
GE-EPI (T2*)								
R1	13	13	13	13	13	13	13	13
R2	30	15	15	15	15	15	15	15
TG	120	123	127	121	118	118	123	126
CF	127746978	127746972	127746969	127746963	127746968	127746964	127746952	127746963
GRE (T2*)								
R1	13	13	13	13	13	13	13	13
R2	15	15	15	15	15	15	15	15
TG	120	126	126	120	119	118	123	126
CF	127746978	127746972	127746969	127746963	127746968	127746964	127746952	127746963

Saline Sample	Pre HLD	Post 10 HLD	Post 20 HLD	Post 30 HLD	Post 40 HLD	Post 50 HLD	Post 60 HLD	Post 70 HLD	Post 80 HLD	Post 90 HLD	Post 100 HLD
SE (T1)											
R1	13	13	13	13	13	13	13	13	13	13	13
R2	30	30	30	30	30	30	30	30	30	30	30
TG	126	128	128	127	126	125	128	125	128	127	124
CF	127746941	127746968	127746960	127746961	127746989	127746993	127746963	127746973	127746982	127746970	127746968
SE (T2)											
R1	13	13	13	13	13	13	13	13	13	13	13
R2	30	30	30	30	30	30	30	30	30	30	30
TG	118	121	122	122	119	120	123	119	124	121	120
CF	127736948	127746968	127746960	127746961	127736989	127746993	127746948	127746973	127746982	127746970	127746968
GE-EPI (T2*)											
R1	13	13	13	13	13	13	13	13	13	13	13
R2	15	15	15	15	15	15	15	15	15	15	15
TG	121	123	124	122	120	119	121	120	123	122	118
CF	127746963	127746968	127746960	127746961	127746989	127746986	127746955	127746973	127746982	127746970	127746968
GRE (T2*)											
R1	13	13	13	13	13	13	13	13	13	13	13
R2	15	15	15	15	15	15	15	15	15	15	15
TG	120	122	129	130	119	119	121	119	127	122	119
CF	127746963	127746968	127746967	127746961	127746989	127746986	127746970	127746973	127746982	127746970	127746968

Bibliography

'(71) STERILITY TESTS.' *USP-NF*. Web. 8 June 2021. GUID-481C30EA-8A49-4A77-9E81-D0CD7C533498_1_en-US

Bangare, Sunil L, Amruta Dubal, Pallavi S Bangare, and ST Patil. 2015. 'Reviewing otsu's method for image thresholding', *International Journal of Applied Engineering Research*, 10: 21777-83.

'Basics of Biosafety Level 2.' *Basics of Biosafety Level 2 | Office of Clinical and Research Safety*, www.vumc.org/safety/bio/basics-biosafety-level-2.

Bill-Axelsson, Anna, Lars Holmberg, Hans Garmo, Jennifer R Rider, Kimmo Taari, Christer Busch, Stig Nordling, Michael Häggman, Swen-Olof Andersson, and Anders Spångberg. 2014. 'Radical prostatectomy or watchful waiting in early prostate cancer', *New England Journal of Medicine*, 370: 932-42.

Borley, Nigel, and Mark R Feneley. 2009. 'Prostate cancer: diagnosis and staging', *Asian journal of andrology*, 11: 74.

Brown, Robert W, Y-C Norman Cheng, E Mark Haacke, Michael R Thompson, and Ramesh Venkatesan. 2014. *Magnetic resonance imaging: physical principles and sequence design* (John Wiley & Sons).

Bushberg, Jerrold T, and John M Boone. 2011. *The essential physics of medical imaging* (Lippincott Williams & Wilkins).

Chen, Bo. 2020. *Fundamentals of Recoupling and Decoupling Techniques in Solid State NMR* (AIP Publishing LLC).

Constantinides, Christakis. 2016. *Magnetic resonance imaging: the basics* (CRC press).

Denmeade, Samuel R, and John T Isaacs. 2002. 'A history of prostate cancer treatment', *Nature Reviews Cancer*, 2: 389-96.

- Gordon, Jeremy W, Rie B Hansen, Peter J Shin, Yesu Feng, Daniel B Vigneron, and Peder EZ Larson. 2018. '3D hyperpolarized C-13 EPI with calibrationless parallel imaging', *Journal of Magnetic Resonance*, 289: 92-99.
- Gruber, Bernhard, Martijn Froeling, Tim Leiner, and Dennis WJ Klomp. 2018. 'RF coils: A practical guide for nonphysicists', *Journal of Magnetic Resonance Imaging*, 48: 590-604.
- Gudbjartsson, Hákon, and Samuel Patz. 1995. 'The Rician distribution of noisy MRI data', *Magnetic resonance in medicine*, 34: 910-14.
- Haider, Masoom A, Axel Krieger, Christine Elliott, Michael R Da Rosa, and Laurent Milot. 2014. 'Prostate imaging: evaluation of a reusable two-channel endorectal receiver coil for MR imaging at 1.5 T', *Radiology*, 270: 556-65.
- Jones, Kyle M, Keith A Michel, James A Bankson, Clifton D Fuller, Ann H Klopp, and Aradhana M Venkatesan. 2018. 'Emerging magnetic resonance imaging technologies for radiation therapy planning and response assessment', *International Journal of Radiation Oncology* Biology* Physics*, 101: 1046-56.
- Kurhanewicz, John, Daniel B Vigneron, Jan Henrik Ardenkjaer-Larsen, James A Bankson, Kevin Brindle, Charles H Cunningham, Ferdia A Gallagher, Kayvan R Keshari, Andreas Kjaer, and Christoffer Laustsen. 2019. 'Hyperpolarized 13C MRI: path to clinical translation in oncology', *Neoplasia*, 21: 1-16.
- Lunt, Sophia Y, and Matthew G Vander Heiden. 2011. 'Aerobic glycolysis: meeting the metabolic requirements of cell proliferation', *Annual review of cell and developmental biology*, 27: 441-64.
- Marieb, Elaine Nicpon, and Katja Hoehn. 2007. *Human anatomy & physiology* (Pearson education).
- Noworolski, Susan M, Jason C Crane, Daniel B Vigneron, and John Kurhanewicz. 2008. 'A clinical comparison of rigid and inflatable endorectal-coil probes for MRI and 3D MR

- spectroscopic imaging (MRSI) of the prostate', *Journal of Magnetic Resonance Imaging: An Official Journal of the International Society for Magnetic Resonance in Medicine*, 27: 1077-82.
- Powell, Daniel K, Karen L Kodsi, Galina Levin, Angela Yim, Duane Nicholson, and Alexander C Kagen. 2014. 'Comparison of comfort and image quality with two endorectal coils in MRI of the prostate', *Journal of Magnetic Resonance Imaging*, 39: 419-26.
- Price, Ron, Jeff Allison, Geoffrey Clarke, Michael Dennis, Edward R. Hendrick, and Carl Keener. 2015. 'MRI Quality Control Manual 2015', *American College of Radiology*: 1-116.
- Pyrek, Kelly. 2012. "Best Practices for High-Level Disinfection and Sterilization of Endoscopes." In *Infection Control Today*. VIRGO Publishing.
- 'SEER*Explorer: An interactive website for SEER cancer statistics '. Accessed 2021.
- The United States Pharmacopeia. The National Formulary. Rockville, Md. :United States Pharmacopeial Convention, Inc., 1979.
- 'Tropon Traceability and Storage Solution.' *Tropon*. Nanosonics, 2021. Web. 15 May 2021. <<https://www.nanosonics.jp/tropon/tropon-traceability-solution/>>.
- Vennesland, Birgit, and Martin E Hanke. 1940. 'The oxidation-reduction potential requirements of a non-spore-forming, obligate anaerobe', *Journal of bacteriology*, 39: 139-69.
- Xu, Bin, Bing Keong Li, Stuart Crozier, Qing Wei, and Feng Liu. 2006. "Model implementation and case study for the lossy, multilayered spherical head phantom in MRI application." In *2005 IEEE Engineering in Medicine and Biology 27th Annual Conference*, 1400-03. IEEE.

Rebecca Rose Feuer DiTusa was born in Baton Rouge, Louisiana, the daughter of Sandra Feuer DiTusa and John Feuer DiTusa. After completing her work at Baton Rouge Magnet High School, Baton Rouge, Louisiana in 2015, she entered Louisiana State University in Baton Rouge, Louisiana. She received the degree of Bachelor of Science with a major in physics and a minor in nuclear science from Louisiana State University in December, 2018. In August of 2019 she entered The University of Texas MD Anderson Cancer Center UTHealth Graduate School of Biomedical Sciences.

Permanent address:

5812 East Fall Creek Parkway North Drive

Indianapolis, IN 46226